

The effect of phase change on stability of convective flow in a layer of volatile liquid driven by a horizontal temperature gradient

Roman O. Grigoriev^{1,†} and Tongran Qin¹

¹School of Physics, Georgia Institute of Technology, Atlanta, GA 30332-0430, USA

(Received 2 April 2017; revised 14 September 2017; accepted 18 December 2017;
first published online 12 January 2018)

Buoyancy–thermocapillary convection in a layer of volatile liquid driven by a horizontal temperature gradient arises in a variety of situations. Recent studies have shown that the composition of the gas phase, which is typically a mixture of vapour and air, has a noticeable effect on the critical Marangoni number describing the onset of convection as well as on the observed convection pattern. Specifically, as the total pressure or, equivalently, the average concentration of air is decreased, the threshold of the instability leading to the emergence of convective rolls is found to increase rather significantly. We present a linear stability analysis of the problem which shows that this trend can be readily understood by considering the transport of heat and vapour through the gas phase. In particular, we show that transport in the gas phase has a noticeable effect even at atmospheric conditions, when phase change is greatly suppressed.

Key words: absolute/convective instability, condensation/evaporation, Marangoni convection

1. Introduction

Convection in fluids with a free surface driven by a horizontal temperature gradient has been studied extensively due to applications in crystal growth and thermal management. The first systematic study of convection in non-volatile fluids appears to be due to Birikh (1966), who derived an analytic solution for a planar return flow in a uniform laterally unbounded layer due to a combination of buoyancy and thermocapillary stresses. This solution also describes the flow away from the end walls in a laterally bounded geometry: thermocapillary stresses drive the flow from the hot end towards the cold end near the free surface, with a return flow near the bottom of the layer. Kirdyashkin (1984) repeated Birikh's theoretical analysis and validated the analytical solutions experimentally.

Smith & Davis (1983*a,b*) performed a linear stability analysis of such flows in the limit of vanishing dynamic Bond number, Bo_D (i.e. ignoring buoyancy effects). They predicted that, depending on the Prandtl number of the liquid, the uniform base flow would undergo an instability towards either surface waves (for $Pr < 0.15$, which corresponds to liquid metals) or hydrothermal waves (for $Pr > 0.15$, which

† Email address for correspondence: romgrig@gatech.edu

corresponds to gases and non-metallic liquids) above a critical Marangoni number Ma , which characterizes the magnitude of thermocapillary stresses. In particular, hydrothermal waves were predicted to form at an angle to the direction of the thermal gradient and travel in the direction of the thermal gradient. As Pr increases, the angle changes smoothly from nearly transverse to nearly parallel to the thermal gradient. The theoretical predictions have since been thoroughly tested and verified both in microgravity and for thin films in terrestrial conditions. A thorough overview of these experiments is presented in a review paper by Schatz & Neitzel (2001).

A different type of instability is found at $Bo_D = O(1)$, when buoyancy is non-negligible. Villers & Platten (1992) studied buoyancy–thermocapillary convection in a rectangular cavity for acetone ($Pr = 4.24$) experimentally and numerically. Although acetone is volatile, reasonable agreement was found between the experimental observations at atmospheric conditions and the numerical simulations based on a one-sided model that ignored heat and mass transfer in the gas phase. For low Ma a featureless planar return flow was found, which is well described by Birikh's solution. At higher Ma a steady cellular pattern featuring multiple convection rolls was found instead of hydrothermal waves. The (transverse) convection rolls were found to rotate in the same direction, unlike the case of pure buoyancy (or Rayleigh–Bénard) convection driven by a vertical temperature gradient. At even higher Ma the steady state was found to be replaced by an oscillatory pattern that was also unlike a hydrothermal wave: the convection rolls were observed to travel in the direction opposite to that of the thermal gradient. Similar results were obtained later by De Saedeleer *et al.* (1996) for decane ($Pr = 15$) and Garcimartín, Mukolobwicz & Daviaud (1997) for 0.65 cSt and 2.0 cSt silicone oil ($Pr = 10$ and 30, respectively) in rectangular cavities with strong confinement in the spanwise direction.

Riley & Neitzel (1998) performed one of the most extensive and detailed experimental studies of convection in 1 cSt silicone oil ($Pr = 13.9$) in a rectangular cavity with a spanwise dimension L_y comparable to the streamwise dimension L_x . They discovered that a direct transition from steady, unicellular flow to hydrothermal waves takes place for small values of the dynamic Bond number ($Bo_D \lesssim 0.2$), while for $Bo_D \gtrsim 0.2$ the results are similar to those of earlier studies with spanwise confinement: the featureless return flow first transitions to steady co-rotating convection cells and, upon further increase in Ma , to an oscillatory multicellular pattern. Riley and Neitzel also determined the critical values of Ma and the wavelength λ of the convective pattern as a function of Bo_D . Burguete *et al.* (2001) performed experiments on convection in 0.65 cSt silicone oil ($Pr = 10.3$) in a rectangular cavity with different aspect ratios where the spanwise dimension was greater than the streamwise dimension. Similarly, they found that the base return flow destabilizes into either oblique travelling waves or longitudinal stationary rolls, respectively, for low and high Bo_D .

Convective patterns have also been studied extensively using numerical simulations. Most of the numerical studies (Ban Hadid & Roux 1990; Ben Hadid & Roux 1992; Villers & Platten 1992; Mundrane & Zebib 1994; Lu & Zhuang 1998; Shevtsova, Nepomnyashchy & Legros 2003) were based on one-sided models which ignore the transport in the gas phase, assume that the free surface is flat and non-deformable, the bottom wall and the interface are adiabatic, and phase change is negligible. These numerical simulations were able to reproduce some features of the experimental studies. For example, Shevtsova *et al.* (2003) and Shevtsova & Legros (2003) performed numerical simulations for decane ($Pr = 14.8$) in a rectangular layer at different Bo_D . They found that as Ma increases, the primary instability leads to

hydrothermal waves for $Bo_D \leq 0.25$, while for $Bo_D \geq 0.32$ the primary (secondary) instability produces a steady (oscillatory) multicellular flow.

Since it does not account for buoyancy, the linear stability analysis of Smith & Davis (1983*a,b*) fails to predict the stationary patterns that emerge for $Bo_D = O(1)$. However, most of the linear stability analyses accounting for buoyancy also failed to predict the correct pattern, i.e. stationary (transverse) rolls that were observed in the experiments. Using adiabatic boundary conditions at the top and bottom of the liquid layer, Parmentier, Regnier & Lebon (1993) predicted transition to travelling waves rather than a steady multicellular pattern for a range of Pr from 0.01 to 10, regardless of the value of Bo_D . Chan & Chen (2010), who used similar assumptions, also predicted transition to travelling waves for a $Pr = 13.9$ fluid. Moreover, their predicted critical Ma and wavelength λ do not match the experiment (Riley & Neitzel 1998). In both cases the predicted travelling waves are oblique for smaller Bo_D and become transverse for Bo_D greater than some critical $O(1)$ value.

Mercier & Normand (1996) showed that transition to a stationary convective pattern can take place if the adiabatic boundary conditions are replaced with Newton's cooling law, although that requires an unrealistically large surface Biot number ($Bi \gtrsim 185/Bo_D$). Moreover, the predicted pattern corresponds to longitudinal convection rolls, while in most experiments transverse rolls were observed. In a subsequent paper Mercier & Normand (2002) considered the effects of the end walls, which they described as spatial disturbances superimposed on the uniform base flow. Their analysis predicted that, depending upon the Prandtl number, convection rolls would develop near the hot end (for $Pr > 4$), near the cold end (for $Pr < 0.01$), or at both end walls (for $0.01 < Pr < 4$).

To our knowledge, the study by Priede & Gerbeth (1997) is the only one to date which correctly predicts the formation of a stationary pattern at $Bo_D = O(1)$. They argued that travelling waves, being convectively unstable, cannot get sufficiently amplified by linear instability in a laterally bounded system. At the same time, the effect of lateral walls extends far into the bulk of the liquid layer, resulting in a stationary pattern of transverse convection rolls. Their predicted critical values of Ma are in reasonable agreement with the threshold values found by Riley & Neitzel (1998), although there is a systematic deviation, suggesting that some important effects have not been considered.

The volatility of the fluids used in the experiments is one source of the discrepancy with analytical (and most numerical) predictions. Although at atmospheric conditions phase change is usually strongly suppressed, it can still play a role. The latent heat associated with phase change can significantly modify the interfacial temperature, and hence the thermocapillary stresses. However, there are very few studies that investigated this effect. Li *et al.* (2012) have studied non-adiabatic effects by using Newton's cooling law with a small Biot number. Their numerical simulations ignored phase change, but were able to reproduce many features of the experimental observations at atmospheric conditions. Ji, Liu & Liu (2008) considered phase change, but ignored buoyancy, so their analysis is only applicable for thin films or under microgravity, i.e. when $Bo_D \approx 0$.

A few recent studies investigated the role played by the gas phase, which is generally a binary mixture of a non-condensable gas (typically air) and the vapour, in more detail. In particular, the experimental study of Li, Grigoriev & Yoda (2014), which used a volatile 0.65 cSt silicone oil ($Pr = 9.2$), showed that for $Bo_D = O(1)$ the threshold values of Ma increase rather dramatically as the air is removed from the experimental apparatus. The numerical simulations of this experimental set-up

(Qin, Tuković & Grigoriev 2014, 2015; Qin & Grigoriev 2015) based on a two-sided model, which took phase change into account and explicitly described the transport of heat and vapour through the gas phase, reproduced the experimental results. The main effect of air is to suppress phase change by impeding the transport of vapour towards, or away from, the interface, but its presence also affects thermal conductivity of the gas layer. This suggests that phase change and transport in the gas phase play an important role in this problem, especially at reduced pressures (reduced concentrations of air).

In order to better understand the mechanism of the instability and the effect of the gas phase we formulated a two-sided model of the flow valid for arbitrary composition of the gas phase; it is described in § 2. The analytical solution describing the uniform return flow (in both phases) is derived in § 3. The stability of that solution is investigated in § 4. The results of linear stability analysis are compared with previous analytical, experimental and numerical studies in § 5, and are discussed in § 6. Conclusions are presented in § 7.

2. Mathematical model

2.1. Governing equations

We will assume that the liquid layer has depth d_l and lateral dimensions much larger than d_l . Since in most experiments the system is covered by a horizontal plate to limit evaporation, we will assume that the gas layer also has a finite depth d_g . To describe convection in this two-layer system, we will use a variation of the two-sided model originally introduced by Qin *et al.* (2014) for near-atmospheric conditions, and later extended by Qin & Grigoriev (2015) to the limit when the gas phase is dominated by the vapour, rather than air. A version of the model interpolating between the two limits is summarized below. The momentum transport in the bulk is described, for both the liquid and the gas phase, by the Navier–Stokes equation

$$\rho(\partial_t \mathbf{u} + \mathbf{u} \cdot \nabla \mathbf{u}) = -\nabla p + \mu \nabla^2 \mathbf{u} + \rho(T, c_a) \mathbf{g}, \quad (2.1)$$

where \mathbf{u} is the fluid velocity, T is the fluid temperature, p is the fluid pressure, ρ and μ are the fluid's density and viscosity, respectively, c_a is the concentration of air, and \mathbf{g} is the gravitational acceleration. (The air is non-condensable, so $c_a = 0$ in the liquid phase.) Following standard practice, we use the Boussinesq approximation, where the density is considered constant everywhere except in the last term on the right-hand side representing the buoyancy force. In particular, the mass conservation equation in both phases reduces to

$$\nabla \cdot \mathbf{u} = 0. \quad (2.2)$$

To account for buoyancy, the density of the liquid phase is assumed to depend linearly on the temperature

$$\rho_l = \rho_l^0 [1 - \beta_l (T - T_0)], \quad (2.3)$$

where ρ_l^0 is the density at the temperature T_0 describing global thermodynamic equilibrium, and $\beta_l = -\rho_l^{-1} \partial \rho_l / \partial T$ is the coefficient of thermal expansion. Here and below, subscripts l , g , v , a and i denote properties of the liquid and gas phase, vapour and air component, and the liquid–vapour interface, respectively. The index 0 will be used throughout the paper to distinguish the equilibrium values from the non-equilibrium ones, where the choice is not obvious. In the gas phase

$$\rho_g = \rho_a + \rho_v, \quad (2.4)$$

where both vapour and air are considered to be ideal gases

$$\rho_{a,v} = \frac{P_{a,v}}{\bar{R}_{a,v}T}, \quad (2.5)$$

$\bar{R}_{a,v} = R/M_{a,v}$, R is the universal gas constant, and $M_{a,v}$ is the molar mass of air/vapour. Correspondingly, the total pressure in the gas is

$$p_g = p_a + p_v. \quad (2.6)$$

Mass transport in the gas phase is described by the standard conservation equation(s)

$$\partial_t n_{a,v} + \nabla \cdot \mathbf{j}_{a,v} = 0, \quad (2.7)$$

for the number density of the two components

$$n_{a,v} = \frac{\rho_{a,v}}{m_{a,v}}, \quad (2.8)$$

where $m_{a,v} = M_{a,v}/N_A$ is the mass of one air/vapour molecule. The number density flux is given by

$$\mathbf{j}_{a,v} = n_{a,v}\mathbf{u} - n_g D \nabla c_{a,v} = n_g(\mathbf{u}c_{a,v} - D \nabla c_{a,v}), \quad (2.9)$$

where the first and the second term on the right-hand side represent the contributions due to advection and diffusion, respectively, D is the binary diffusion coefficient, and

$$c_{a,v} = \frac{n_{a,v}}{n_g} = \frac{P_{a,v}}{p_g} \quad (2.10)$$

are the concentrations (or, more precisely, the molar fractions) of the two components. Therefore, the conservation equation(s) (2.7) can be rewritten as

$$\partial_t(n_g c_{a,v}) + n_g \mathbf{u} \cdot \nabla c_{a,v} = \nabla \cdot (n_g D \nabla c_{a,v}). \quad (2.11)$$

From the ideal gas law, the total number density in the gas phase

$$n_g = \frac{p_g}{k_B T}, \quad (2.12)$$

where $k_B = R/N_A$ is the Boltzmann constant. As we showed previously (Qin *et al.* 2015), spatial variation of p_g can in practice be neglected. Furthermore, the largest temperature variation in relevant experimental and numerical studies is around 5% (and typically much smaller than that), such that n_g can be assumed constant. Consequently (2.11) reduces to an advection–diffusion equation for the two concentrations

$$\partial_t c_{a,v} + \mathbf{u} \cdot \nabla c_{a,v} = \nabla \cdot (D \nabla c_{a,v}). \quad (2.13)$$

These two equations are equivalent, so either one can be used, since $c_a + c_v = 1$.

Finally, the transport of heat is also described using an advection–diffusion equation

$$\partial_t T + \mathbf{u} \cdot \nabla T = \alpha \nabla^2 T, \quad (2.14)$$

where $\alpha = k/(\rho C_p)$ is the thermal diffusivity, k is the thermal conductivity, and C_p is the heat capacity, of the fluid.

2.2. Boundary conditions at the interface

The system of coupled evolution equations for the velocity, pressure, temperature and concentration fields should be solved in a self-consistent manner, subject to the boundary conditions describing the balance of momentum, heat and mass fluxes between the two phases. The phase change at the interface can be described using kinetic theory (Schrage 1953). As we have shown previously (Qin *et al.* 2015), the choice of the phase change model has negligible effect on the results. The mass flux across the interface is given by (Klentzman & Ajaev 2009)

$$J = \frac{2\chi}{2 - \chi} \rho_v \sqrt{\frac{\bar{R}_v T_i}{2\pi}} \left[\frac{p_l - p_g}{\rho_l \bar{R}_v T_i} + \frac{\mathcal{L}}{\bar{R}_v T_i} \frac{T_i - T_s}{T_s} \right], \tag{2.15}$$

where χ is the accommodation coefficient, \mathcal{L} is the latent heat of vaporization, and subscript s denotes saturation values for the vapour. The dependence of the local saturation temperature T_s on the partial pressure of vapour p_v is described using the Clausius–Clapeyron equation for phase equilibrium

$$\ln \frac{p_v}{p_v^0} = \frac{\mathcal{L}}{\bar{R}_v} \left[\frac{1}{T_0} - \frac{1}{T_s} \right], \tag{2.16}$$

where p_v^0 is the saturation pressure of the vapour at the equilibrium temperature T_0 . The first term in (2.15) is proportional to the Young–Laplace pressure and can be ignored in this problem, since the interface is considered flat.

The mass flux balance at the interface can be expressed with the help of (2.7). In the reference frame of the interface, the mass flux of the vapour is given by

$$\frac{J}{m_v} = \hat{n} \cdot \mathbf{j}_v = n_g \hat{n} \cdot ([\mathbf{u}_g - \mathbf{u}_i]c_v - D\nabla c_v), \tag{2.17}$$

where \mathbf{u}_i is the velocity of the liquid at the interface and \hat{n} is the unit vector normal to the interface. Since air is non-condensable, its mass flux across the interface is zero:

$$0 = \hat{n} \cdot \mathbf{j}_a = n_g \hat{n} \cdot ([\mathbf{u}_g - \mathbf{u}_i]c_a - D\nabla c_a). \tag{2.18}$$

Since $c_a + c_v = 1$, these two relations can be solved yielding two of the boundary conditions for (2.1) and (2.7) in the gas phase

$$\hat{n} \cdot \nabla c_v = -\frac{c_a J}{m_v n_g D} \tag{2.19}$$

and

$$\hat{n} \cdot (\mathbf{u}_g - \mathbf{u}_i) = \frac{J}{m_v n_g}. \tag{2.20}$$

The heat flux balance is given by

$$\mathcal{L}J = \hat{n} \cdot k_g \nabla T_g - \hat{n} \cdot k_l \nabla T_l, \tag{2.21}$$

where the advective contribution to the heat flux is negligible on both sides of the interface. Indeed, in the gas phase, conduction is the dominant contribution (Qin & Grigoriev 2015), while on the liquid side

$$\hat{n} \cdot (\mathbf{u}_l - \mathbf{u}_i) = \frac{J}{\rho_l}. \tag{2.22}$$

Since the liquid density is much greater than that of the gas, the left-hand side of (2.22) is very small compared with $\hat{\mathbf{n}} \cdot (\mathbf{u}_g - \mathbf{u}_l)$ and can be ignored.

The remaining boundary conditions for \mathbf{u} and T at the liquid–vapour interface are standard: the temperature is continuous

$$T_l = T_i = T_v \quad (2.23)$$

as are the tangential velocity components

$$(\mathbb{I} - \hat{\mathbf{n}}\hat{\mathbf{n}}) \cdot (\mathbf{u}_l - \mathbf{u}_g) = 0. \quad (2.24)$$

The stress balance

$$(\boldsymbol{\Sigma}_l - \boldsymbol{\Sigma}_g) \cdot \hat{\mathbf{n}} = \hat{\mathbf{n}}\kappa\sigma - \gamma \nabla_s T_i \quad (2.25)$$

incorporates both the viscous drag between the two phases and the thermocapillary effect. Here $\boldsymbol{\Sigma} = \mu[\nabla\mathbf{u} + (\nabla\mathbf{u})^T] - p$ is the stress tensor, $\kappa (= 0)$ is the interfacial curvature, $\nabla_s = (\mathbb{I} - \hat{\mathbf{n}}\hat{\mathbf{n}}) \cdot \nabla$ is the surface gradient, and $\gamma = -\partial\sigma/\partial T$ is the temperature coefficient of surface tension.

We will further assume that side/top/bottom walls are adiabatic, $\hat{\mathbf{n}} \cdot \nabla T = 0$, which is a good approximation for most experimental set-ups. The heat transport through the end walls at $x=0$ and $x=L_x$ is not treated explicitly in this study, but in principle a variety of boundary conditions, from constant temperature to constant flux to mixed boundary conditions can be accommodated. Standard no-slip boundary conditions $\mathbf{u} = 0$ for the velocity and no-flux boundary conditions $\hat{\mathbf{n}} \cdot \nabla c_{a,v} = 0$ for concentration apply on all the walls.

3. The base flow

In liquid layers that are not too thin, under normal gravity, convection is driven by both buoyancy and thermocapillarity. The strength of these two effects can be quantified, respectively, in terms of the Marangoni number

$$Ma = \frac{\gamma d_l^2}{\mu_l \alpha_l} \tau \quad (3.1)$$

and the Rayleigh number

$$Ra = \frac{g \beta_l d_l^4 \tau}{\nu_l \alpha_l}, \quad (3.2)$$

where $\nu_l = \mu_l/\rho_l$ is the kinematic viscosity of the liquid and τ is the horizontal component of the temperature gradient, assumed to be in the positive x direction. In the numerics and experiment we set $\tau = \hat{\mathbf{x}} \cdot \nabla_s T_i$, which is found to be nearly independent of the location in the central region of the flow (Qin & Grigoriev 2015). The dynamic Bond number

$$Bo_D = \frac{Ra}{Ma} = \frac{\rho_l g \beta_l d_l^2}{\gamma} \quad (3.3)$$

is independent of τ and quantifies the relative strength of buoyancy and thermocapillarity. In defining non-dimensional combinations, as well as various scales, we will use the values of material parameters at the equilibrium temperature T_0 .

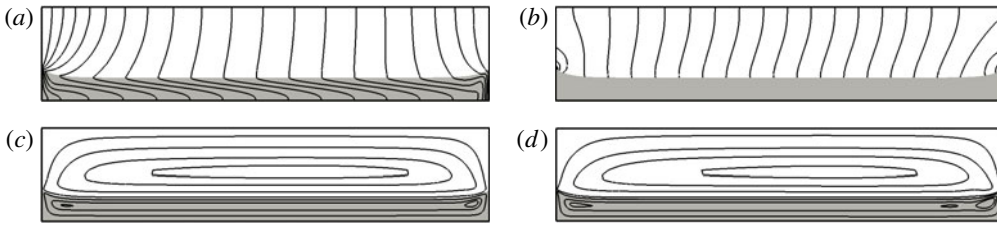


FIGURE 1. Numerical solutions at $c_a^0 = 0.96$ (atmospheric conditions) for the flow of 0.65 cSt silicone oil in a rectangular cell with aspect ratios $\Gamma_x = 19.4$ and $A = 3$ (Qin & Grigoriev 2015). Shown are the level sets of (a) the temperature field T , (b) vapour concentration field c_v , and (c) stream function ψ for $Ma = 190$. (d) Shows the streamlines for a slightly higher $Ma = 370$. Here and below, the grey (white) background indicates the liquid (gas) phase. The horizontal and vertical axes are x and z ; the cold/hot end wall is on the left/right.

As discussed in the introduction, at sufficiently low Ma , a steady return flow is found in the liquid layer. The analytical solution of Birikh (1966) describes such a flow in laterally unbounded layers of non-volatile liquids. This solution also describes the flow observed in laterally bounded layers away from the end walls (cf. figure 1) even for volatile fluids under atmospheric conditions when the phase change is strongly suppressed (Qin *et al.* 2014). For volatile fluids at reduced pressures, Birikh’s solution becomes invalid due to the increasing role of phase change (Li *et al.* 2014; Qin *et al.* 2014). Instead, we should look for a solution to the two-sided model described in the previous section, which describes the flow in both layers. In order to reduce the number of parameters, the governing equations (2.1), (2.2), (2.13), and (2.14) are non-dimensionalized by introducing the length scale d_l , time scale d_l^2/ν_l , velocity scale ν_l/d_l , density scale ρ_l , pressure scale $\rho_l(\nu_l/d_l)^2$, and temperature scale $\tau d_l = \mu_l \alpha_l Ma / (\gamma d_l)$.

The dimensionless governing equations for the liquid layer become

$$\left. \begin{aligned} \tilde{\nabla} \cdot \tilde{\mathbf{u}}_l &= 0, \\ \partial_{\tilde{t}} \tilde{\mathbf{u}}_l + \tilde{\mathbf{u}}_l \cdot \tilde{\nabla} \tilde{\mathbf{u}}_l &= -\tilde{\nabla} \tilde{p} + \tilde{\nabla}^2 \tilde{\mathbf{u}}_l + Gr \tilde{T}_l \hat{z}, \\ \partial_{\tilde{t}} \tilde{T}_l + \tilde{\mathbf{u}}_l \cdot \tilde{\nabla} \tilde{T}_l &= Pr^{-1} \tilde{\nabla}^2 \tilde{T}_l, \end{aligned} \right\} \quad (3.4)$$

where $\tilde{\nabla} = d_l \nabla$, $\tilde{\mathbf{u}}_l = \mathbf{u}_l d_l / \nu_l$, $\tilde{T}_l = (T_l - T_0) / (\tau d_l)$, and

$$Gr = \frac{Ra}{Pr} = \frac{g \beta_l d_l^4 \tau}{\nu_l^2} \quad (3.5)$$

is the Grashof number. We will use a coordinate system defined such that the liquid–vapour interface corresponds to the plane $\tilde{z} = 0$ (so that the liquid layer corresponds to $-1 < \tilde{z} < 0$). Recall that the x axis points in the direction of the applied temperature gradient, with the origin chosen such that $T_i = T_0$ at $\tilde{x} = 0$.

The dimensionless governing equations for the gas layer ($0 < \tilde{z} < A$) are

$$\left. \begin{aligned} \tilde{\nabla} \cdot \tilde{\mathbf{u}}_g &= 0, \\ \partial_{\tilde{t}} \tilde{\mathbf{u}}_g + \tilde{\mathbf{u}}_g \cdot \tilde{\nabla} \tilde{\mathbf{u}}_g &= -\frac{\rho_l}{\rho_g} \tilde{\nabla} \tilde{p} + K_v \tilde{\nabla}^2 \tilde{\mathbf{u}}_g + (\mathcal{E}_T \tilde{T}_g + \mathcal{E}_c \tilde{c}_v) \hat{z}, \\ \partial_{\tilde{t}} \tilde{T}_g + \tilde{\mathbf{u}}_g \cdot \tilde{\nabla} \tilde{T}_g &= K_\alpha \tilde{\nabla}^2 \tilde{T}_g, \\ \partial_{\tilde{t}} \tilde{c}_v + \tilde{\mathbf{u}}_g \cdot \tilde{\nabla} \tilde{c}_v &= K_D \tilde{\nabla}^2 \tilde{c}_v, \end{aligned} \right\} \quad (3.6)$$

where $\tilde{\mathbf{u}}_g = \mathbf{u}_g d_l / \nu_l$, $\tilde{T}_g = (T_g - T_0) / (\tau d_l)$, $\tilde{c}_v = c_v - c_v^0$, $c_v^0 = 1 - c_a^0$, $A = d_g / d_l$, $K_v = \nu_g / \nu_l$, $K_\alpha = \alpha_g / \nu_l$, and $K_D = D / \nu_l$. The non-dimensional combinations

$$\left. \begin{aligned} \mathcal{E}_T &= \frac{g \beta_g d_l^4 \tau}{\nu_l^2} = \frac{\beta_g}{\beta_l} Gr, \\ \mathcal{E}_c &= \frac{g d_l^3}{\nu_l^2} \frac{m_a - m_v}{c_a^0 m_a + c_v^0 m_v}, \end{aligned} \right\} \tag{3.7}$$

describe the contributions to the buoyancy force in the gas layer due to perturbations in the temperature and composition of the gas, respectively. Note that \mathcal{E}_T depends on the imposed temperature gradient τ , but not c_a^0 , while \mathcal{E}_c depends on c_a^0 , but not τ .

Both the imposed temperature gradient τ and the composition of the gas phase, parametrized by the equilibrium concentration of air c_a^0 , play a key role in this problem. In experiment (Li *et al.* 2014), c_a^0 was controlled indirectly by varying the net gas pressure

$$p_g^0 = \frac{p_v^0}{1 - c_a^0}. \tag{3.8}$$

In the following analysis, it will be more convenient to describe the composition directly in terms of c_a^0 . In terms of p_g^0 , we can write $n_g \approx p_g^0 / (k_B T_0)$, while \tilde{p} in (3.4) and (3.6) represents the non-dimensional form of the difference $p_g - p_g^0$.

In order to satisfy the incompressibility condition, we will assume that the flow is strictly two-dimensional and introduce a stream function for each layer, such that

$$\left. \begin{aligned} \tilde{\mathbf{u}}_l &= (\partial_z \tilde{\psi}_l, 0, -\partial_x \tilde{\psi}_l), \\ \tilde{\mathbf{u}}_g &= (\partial_z \tilde{\psi}_g, 0, -\partial_x \tilde{\psi}_g). \end{aligned} \right\} \tag{3.9}$$

Eliminating the pressure, the governing equations (3.4) for the liquid layer can be rewritten as

$$\left. \begin{aligned} (\partial_t - \tilde{\nabla}^2 + \partial_z \tilde{\psi}_l \partial_x - \partial_x \tilde{\psi}_l \partial_z) \tilde{\nabla}^2 \tilde{\psi}_l + Gr \partial_x \tilde{T}_l &= 0, \\ \partial_t \tilde{T}_l + \partial_z \tilde{\psi}_l \partial_x \tilde{T}_l - \partial_x \tilde{\psi}_l \partial_z \tilde{T}_l - Pr^{-1} \tilde{\nabla}^2 \tilde{T}_l &= 0. \end{aligned} \right\} \tag{3.10}$$

For the gas layer we have

$$\left. \begin{aligned} (\partial_t - K_v \tilde{\nabla}^2 + \partial_z \tilde{\psi}_g \partial_x - \partial_x \tilde{\psi}_g \partial_z) \tilde{\nabla}^2 \tilde{\psi}_g + \mathcal{E}_T \partial_x \tilde{T}_g + \mathcal{E}_c \partial_z \tilde{c}_v &= 0, \\ \partial_t \tilde{T}_g + \partial_z \tilde{\psi}_g \partial_x \tilde{T}_g - \partial_x \tilde{\psi}_g \partial_z \tilde{T}_g - K_\alpha \tilde{\nabla}^2 \tilde{T}_g &= 0, \\ \partial_t \tilde{c}_v + \partial_z \tilde{\psi}_g \partial_x \tilde{c}_v - \partial_x \tilde{\psi}_g \partial_z \tilde{c}_v - K_D \tilde{\nabla}^2 \tilde{c}_v &= 0. \end{aligned} \right\} \tag{3.11}$$

3.1. Boundary conditions

At the bottom of the liquid layer ($\tilde{z} = -1$) and the top of the gas layer ($\tilde{z} = A$), no-slip and adiabatic boundary conditions apply

$$\left. \begin{aligned} \tilde{\mathbf{u}} &= 0, \\ \partial_z \tilde{T} &= 0. \end{aligned} \right\} \tag{3.12}$$

At the interface ($\tilde{z} = 0$), the temperature and velocity fields are continuous

$$\left. \begin{aligned} \tilde{T}_l &= \tilde{T}_g = \tilde{T}_i, \\ \tilde{\mathbf{u}}_l &= \tilde{\mathbf{u}}_g = \tilde{\mathbf{u}}_i, \end{aligned} \right\} \tag{3.13}$$

where for our choice of the origin of coordinate system $\tilde{T}_i = \tilde{x}$. Since $\mu_l \gg \mu_g$ and typically $d_g > d_l$, the viscous stress in the gas layer can be ignored, yielding a simplified expression for the shear stress balance at the interface

$$\partial_z \tilde{u}_{l,x} = -Re \partial_x \tilde{T}_l, \tag{3.14}$$

where

$$Re = \frac{Ma}{Pr} = \frac{\gamma d_l^2}{\mu_l \nu_l} \tau \tag{3.15}$$

is the Reynolds number.

The heat flux balance (2.21) at the interface reduces to

$$\partial_z \tilde{T}_l = \frac{k_g}{k_l} \partial_z \tilde{T}_g - \frac{V}{Ma} \tilde{J}, \tag{3.16}$$

where $k_g = c_v^0 k_v + c_a^0 k_a$, and $\tilde{J} = Jd_l / (Dm_v n_g)$ is the dimensionless mass flux. The dimensionless combination

$$V = \frac{\mathcal{L} \gamma d_l}{\alpha_l \mu_l k_l} \frac{Dp_g^0}{R_v T_0}, \tag{3.17}$$

or more precisely the ratio V/Ma , describes the relative magnitude of the latent heat released (absorbed) at the interface due to condensation (evaporation) compared with the vertical heat flux in the liquid layer due to conduction. It should be noted that, although the product Dp_g^0 , and consequently V , is a function of T_0 , it is independent of the gas pressure, and therefore c_a^0 .

Non-dimensionalizing (2.19) and (2.20), we obtain

$$\partial_z \tilde{c}_v = -c_a^0 c_v^0 \tilde{J}, \tag{3.18}$$

and

$$\hat{n} \cdot (\tilde{\mathbf{u}}_g - \tilde{\mathbf{u}}_l) = c_v^0 K_D \tilde{J}. \tag{3.19}$$

The mass flux vanishes at the top of the gas layer

$$\partial_z \tilde{c}_v = 0. \tag{3.20}$$

The base uniform flow corresponds to a vanishing mass flux at the interface, $\tilde{J} = 0$, which is also an assumption made by all one-sided models. The base flow is spatially uniform in the lateral direction(s) which, coupled with incompressibility, requires $\hat{n} \cdot \mathbf{u}_i = 0$. This leads to a number of simplifications. In particular, (3.18) and (3.19) require that $\tilde{u}_{l,z} = \tilde{u}_{g,z} = 0$ and $\partial_z \tilde{c}_v = 0$ at the interface. Furthermore, the heat flux at the interface should also vanish, so that (2.21) gives $\partial_z \tilde{T}_l = \partial_z \tilde{T}_g = 0$.

The boundary conditions for the stream function can be easily obtained from those for the velocities. At the bottom of the liquid layer and the top of the gas layer

$$\left. \begin{aligned} \tilde{\psi} &= 0, \\ \partial_x \tilde{\psi} &= \partial_z \tilde{\psi} = 0. \end{aligned} \right\} \tag{3.21}$$

For a uniform flow, the net flux through any vertical plane vanishes. Combined with conditions (2.24) and (2.25) this requires that at the interface

$$\left. \begin{aligned} \tilde{\psi}_l &= \tilde{\psi}_g = 0, \\ \partial_z \tilde{\psi}_l - \partial_z \tilde{\psi}_g &= 0, \\ \partial_z^2 \tilde{\psi}_l + Re \partial_x \tilde{T}_l &= 0. \end{aligned} \right\} \tag{3.22}$$

3.2. Fluid flow and temperature in the liquid layer

For a uniform horizontal flow, where both $\tilde{\psi}_l$ and $\tilde{\psi}_g$ are functions of \tilde{z} alone, we can look for solutions to (3.10) in the form

$$\tilde{T}_l = \tilde{x} + \tilde{\theta}_l(\tilde{z}), \quad (3.23)$$

where $\tilde{\theta}_l(0) = 0$. With this choice, the system (3.10) reduces to coupled ordinary differential equations (ODEs)

$$\left. \begin{aligned} -\tilde{\psi}_l'''' + Gr = 0, \\ Pr \tilde{\psi}_l' - \tilde{\theta}_l'' = 0, \end{aligned} \right\} \quad (3.24)$$

where prime stands for the derivatives with respect to the \tilde{z} coordinate.

Solving the system (3.24) subject to the boundary conditions at the bottom and the free surface of the liquid layer, we find the steady-state solutions for the stream function

$$\tilde{\psi}_l = Re \left[-\frac{\tilde{z}(\tilde{z} + 1)^2}{4} + Bo_D \frac{\tilde{z}(\tilde{z} + 1)^2(2\tilde{z} - 1)}{48} \right], \quad (3.25)$$

velocity

$$\tilde{u}_l = Re \left[-\frac{(\tilde{z} + 1)(3\tilde{z} + 1)}{4} + Bo_D \frac{(\tilde{z} + 1)(8\tilde{z}^2 + \tilde{z} - 1)}{48} \right] \hat{x}, \quad (3.26)$$

and temperature field

$$\tilde{T}_l = \tilde{x} + Ma \left[-\frac{\tilde{z}^2(3\tilde{z}^2 + 8\tilde{z} + 6)}{48} + Bo_D \frac{\tilde{z}^2(8\tilde{z}^3 + 15\tilde{z}^2 - 10)}{960} \right], \quad (3.27)$$

describing the base flow. They agree with the analytical solutions originally obtained by Birikh (1966) and later rederived by Kirdyashkin (1984) and Villers & Platten (1987) using a one-sided model that ignores the effects of the gas phase.

The assumption that the interfacial temperature varies linearly has been widely used in previous studies, without much justification, for deriving the solutions (3.26) and (3.27) for the return flow underlying the stability analyses (Parmentier *et al.* 1993; Mercier & Normand 1996; Priede & Gerbeth 1997) as well as in models of the adiabatic section of heat pipes (Ha & Peterson 1994; Suman & Kumar 2005; Markos, Ajaev & Homsy 2006), which assume unidirectional flow in the liquid phase. However, the validity of this assumption cannot be established by a one-sided model which ignores heat and mass transport in the gas phase. In fact, when c_a^0 becomes sufficiently low, the interfacial temperature profile becomes nonlinear (Li *et al.* 2014; Qin & Grigoriev 2015). Proper justification of the linearity assumption requires showing that it is consistent with a steady-state solution of the transport equations in the gas phase, which satisfies all of the boundary conditions at the free surface. We turn to this next.

3.3. Fluid flow, temperature and composition in the gas layer

The solutions for the velocity, temperature and composition of the gas phase can be found in the same way the solutions (3.26) and (3.27) were obtained for the liquid phase. We will start by finding the solution for the vapour concentration at the interface before deriving the solution in the bulk. Since there is no phase

change, $T_s = T_i$, according to (2.15), and $\partial_x T_s = \tau$. Using the Clausius–Clapeyron relation (2.16) and neglecting the deviation of p_g from the equilibrium value (3.8) we therefore find

$$\partial_x c_v = \frac{\mathcal{L}\tau}{\bar{R}_v T_i^2} c_v, \tag{3.28}$$

where for $\tau x \ll T_0$ we can replace T_i with the equilibrium temperature T_0 . In general, the solution to this equation yields an exponential concentration profile for c_v and hence a nonlinear interfacial temperature profile (Qin & Grigoriev 2015). However, when the deviation of c_v from c_v^0 is small, the concentration profile at the interface becomes approximately linear

$$\tilde{c}_v \approx \Omega \tilde{x}, \tag{3.29}$$

where

$$\Omega = c_v^0 \frac{\mathcal{L}d_l\tau}{\bar{R}_v T_0^2} = c_v^0 \frac{H}{V} Ma, \tag{3.30}$$

and

$$H = \frac{\mathcal{L}^2 D p_g^0}{\bar{R}_v^2 T_0^3 k_l} \tag{3.31}$$

is another non-dimensional parameter, the meaning of which will become clear later. Again, since the product $D p_g^0$ is independent of c_a^0 , so is H .

Given the boundary conditions for \tilde{T}_g and \tilde{c}_v , we can look for solutions to these two fields in the gas layer of the form

$$\left. \begin{aligned} \tilde{T}_g &= \tilde{x} + \tilde{\theta}_g(\tilde{z}), \\ \tilde{c}_v &= \Omega[\tilde{x} + \tilde{\zeta}_v(\tilde{z})], \end{aligned} \right\} \tag{3.32}$$

where

$$\left. \begin{aligned} \tilde{\theta}_g(0) &= 0, \\ \tilde{\zeta}_v(0) &= 0. \end{aligned} \right\} \tag{3.33}$$

For a uniform flow, $\tilde{\psi}_g$ should only depends on \tilde{z} , so the system (3.11) reduces to

$$\left. \begin{aligned} -\tilde{\psi}_g'''' + \mathcal{E}_T + \mathcal{E}_c \Omega &= 0, \\ \tilde{\psi}_g' - K_\alpha \tilde{\theta}_g'' &= 0, \\ \tilde{\psi}_g' - K_D \tilde{\zeta}_v'' &= 0. \end{aligned} \right\} \tag{3.34}$$

Solving these equations subject to the boundary conditions (3.20), (3.21), (3.22) and (3.33) at the interface and the top of the gas layer yields the steady-state solutions for the stream function

$$\tilde{\psi}_g = -\mathcal{R} \left[\frac{\tilde{z}(\tilde{z} - A)^2}{4A^2} + \mathcal{B} \frac{\tilde{z}(\tilde{z} - A)^2(2\tilde{z} + A)}{48A^3} \right], \tag{3.35}$$

velocity

$$\tilde{u}_g = -\mathcal{R} \left[\frac{(\tilde{z} - A)(3\tilde{z} - A)}{4A^2} + \mathcal{B} \frac{(\tilde{z} - A)(8\tilde{z}^2 - A\tilde{z} - A^2)}{48A^3} \right] \hat{x}, \tag{3.36}$$

temperature

$$\tilde{T}_g = \tilde{x} - \frac{\mathcal{R}}{K_\alpha} \left[\frac{\tilde{z}^2(3\tilde{z}^2 - 8A\tilde{z} + 6A^2)}{48A^2} + \mathcal{B} \frac{\tilde{z}^2(8\tilde{z}^3 - 15A\tilde{z}^2 + 10A^3)}{960A^3} \right], \tag{3.37}$$

and vapour concentration in the gas phase

$$\tilde{c}_v = \Omega\tilde{x} - \Omega \frac{\mathcal{R}}{K_D} \left[\frac{\tilde{z}^2(3\tilde{z}^2 - 8A\tilde{z} + 6A^2)}{48A^2} + \mathcal{B} \frac{\tilde{z}^2(8\tilde{z}^3 - 15A\tilde{z}^2 + 10A^3)}{960A^3} \right]. \tag{3.38}$$

The parameters \mathcal{R} and \mathcal{B} are analogous to the Reynolds number and the dynamic Bond number, but incorporate the properties of both fluid layers:

$$\left. \begin{aligned} \mathcal{R} &= Re \left(1 + \frac{Bo_D}{12} \right) + \frac{A^3}{12K_v} (\mathcal{E}_T + \mathcal{E}_c), \\ \mathcal{B} &= -\frac{A^3}{\mathcal{R}K_v} (\mathcal{E}_T + \mathcal{E}_c), \end{aligned} \right\} \tag{3.39}$$

where we defined

$$\mathcal{E}_c = \mathcal{E}_c \Omega = -\frac{(1 - c_a^0)(\bar{R}_a - \bar{R}_v)}{\bar{R}_a - (\bar{R}_a - \bar{R}_v)c_a^0} \frac{\mathcal{L}Bo_D}{\beta_l \bar{R}_v T^2} \frac{Ma}{Pr}. \tag{3.40}$$

Note that the form of the analytical solutions (3.26)–(3.27) and (3.36)–(3.38) is different from that of the solutions derived by Qin *et al.* (2014) because (i) the buoyancy force caused by the variation in the composition of the gas is explicitly taken into account in the present analysis, (ii) the mass transport in the gas phase is described using the concentration rather than the mass density of the vapour, and (iii) a different choice of the origin of the coordinate system is made. Figure 2 compares the analytical solutions with the numerical ones (cf. figure 1) computed by Qin & Grigoriev (2015). We find that the analytical solutions accurately describe the core region of the flow away from the end walls for sufficiently low τ at which the base flow is stable.

4. Linear stability analysis

The main focus of our study is on relatively thick layers where the effect of buoyancy is non-negligible, such that $Bo_D = O(1)$. In this parameter regime gravity is strong enough to keep the liquid interface nearly flat, so in our analysis we will assume that the thickness of the liquid layer remains uniform even after the onset of the convection pattern. To date, only one study (Priede & Gerbeth 1997) of pattern formation in buoyancy–thermocapillary convection correctly predicted the formation of a stationary pattern of convection rolls observed in experiment at $Bo_D = O(1)$. This study was based on a one-sided model which completely ignored phase change and assumed adiabatic conditions at the free surface. While such description may be acceptable for non-volatile liquids or at high concentrations of air, it fails to describe volatile liquids at lower concentrations of air. Below a generalized analysis is presented, which accounts for both heat and mass flux across the interface associated with phase change and which is applicable regardless of the amount of air present in the gas layer (quantified by c_a^0).

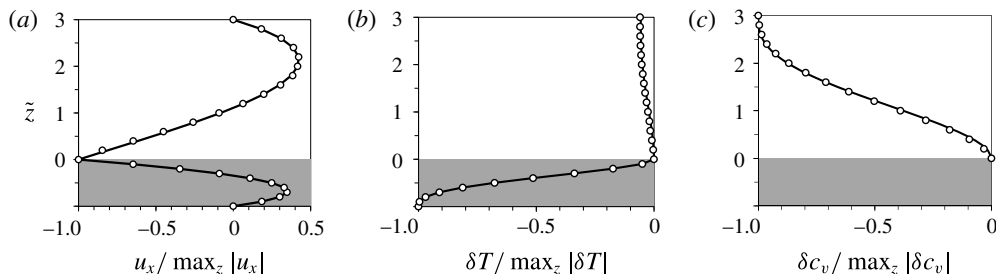


FIGURE 2. Comparison between the numerical and analytical solutions for $Ma=190$ and $c_a^0=0.96$ (atmospheric conditions) in the middle of the cell, $x=L_x/2$. Shown are the normalized vertical profiles of (a) the horizontal velocity $u_x = u_x$, (b) the variation $\delta T = T - T_i$ of the temperature, and (c) the variation $\delta c_v = c_v - c_{v,i}$ of vapour concentration. Open circles correspond to numerical results and solid lines correspond to the analytical solutions.

4.1. Diffusion-dominated case

While the non-dimensional equations (3.4) for the liquid layer can be used without modification, in order to obtain a simplified problem, which can generate useful physical insight, we will start by making several approximations in the treatment of heat and mass transport on the gas side. The relative contribution of advection and diffusion to the mass and heat transport in the gas layer are described by the Péclet numbers Pe_m and Pe_t , respectively. Since the relevant length scale here is the wavelength of the convective pattern, which is comparable to the depth of the liquid layer, and the velocity scale is determined by the interfacial velocity $u_i = v_l \tilde{u}_l(0)/d_l$ (cf. (3.26)), we have

$$Pe_m = \frac{|u_i|d_l}{D} = \frac{12 + Bo_D}{48} \frac{Re}{K_D}, \tag{4.1}$$

and

$$Pe_t = \frac{|u_i|d_l}{\alpha_g} = \frac{12 + Bo_D}{48} \frac{Re}{K_\alpha}. \tag{4.2}$$

In typical experiments (Villers & Platten 1992; Riley & Neitzel 1998; Li *et al.* 2014) both Péclet numbers are at most $O(1)$, so we can drop the advective terms in the transport equations (2.13) and (2.14) in the gas phase. Furthermore, if we are only interested in the transition thresholds for stationary instability, we can also ignore the time derivatives, such that the system (3.11) simplifies to

$$\left. \begin{aligned} \tilde{\psi}_g &= 0, \\ (\partial_x^2 + \partial_z^2)\tilde{T}_g &= 0, \\ (\partial_x^2 + \partial_z^2)\tilde{c}_v &= 0. \end{aligned} \right\} \tag{4.3}$$

Note that neglecting the transient dynamics of the gas phase changes neither the critical Marangoni number nor the critical wavelength of a (stationary) pattern.

The base solution $\tilde{\psi}_{l0}, \tilde{T}_{l0}$ describing the uniform return flow in the liquid layer is given by (3.25)–(3.27). The base solution to (4.3) describing the gas layer in the diffusion-dominated case can be obtained by setting $\mathcal{R} = 0$ in (3.37)–(3.38), which is

equivalent to setting $\tilde{\mathbf{u}}_g = 0$ ($\tilde{\psi}_g = 0$) and gives:

$$\left. \begin{aligned} \tilde{T}_{g0} &= \tilde{x}, \\ \tilde{c}_{v0} &= \Omega \tilde{x}. \end{aligned} \right\} \tag{4.4}$$

Although the base state satisfies the adiabatic boundary condition at the interface, perturbations in the temperature will give rise to heat and mass flux across the interface and, consequently, through the gas phase. Perturbed solutions can be written in the form of Fourier integrals

$$\left. \begin{aligned} \tilde{\psi}_m &= \tilde{\psi}_{m0} + \int_{-\infty}^{\infty} \tilde{\psi}_{mq}(\tilde{z}) e^{iqx + \sigma_q t} dq, \\ \tilde{T}_m &= \tilde{T}_{m0} + \int_{-\infty}^{\infty} \tilde{\theta}_{mq}(\tilde{z}) e^{iqx + \sigma_q t} dq, \\ \tilde{c}_v &= \tilde{c}_{v0} + \Omega \int_{-\infty}^{\infty} \tilde{\zeta}_{vq}(\tilde{z}) e^{iqx + \sigma_q t} dq, \end{aligned} \right\} \tag{4.5}$$

where $m = \{l, g\}$ denotes the phase, q is the wavenumber describing the variation in the horizontal direction, and σ_q is the temporal growth rate. The functions $\tilde{\psi}_{mq}(\tilde{z})$, $\tilde{\theta}_{mq}(\tilde{z})$, and $\tilde{\zeta}_{vq}(\tilde{z})$ define the vertical profile for the perturbations in, respectively, the stream function $\tilde{\psi}$, temperature \tilde{T} , and vapour concentration \tilde{c}_v with wavenumber q .

Rewriting (4.3) in terms of the perturbations, we obtain

$$\left. \begin{aligned} \tilde{\psi}_{gq} &= 0, \\ \tilde{\theta}_{gq}'' &= q^2 \tilde{\theta}_{gq}, \\ \tilde{\zeta}_{vq}'' &= q^2 \tilde{\zeta}_{vq}. \end{aligned} \right\} \tag{4.6}$$

Temperature continuity at the interface requires

$$\tilde{\theta}_{gq}(0) = \tilde{\theta}_{lq}(0). \tag{4.7}$$

At the top of the gas layer we have

$$\left. \begin{aligned} \tilde{\theta}'_{gq}(A) &= 0, \\ \tilde{\zeta}'_{vq}(A) &= 0. \end{aligned} \right\} \tag{4.8}$$

The solution of (4.6) satisfying these boundary conditions is

$$\tilde{\theta}_{gq}(\tilde{z}) = \frac{\cosh[q(\tilde{z} - A)]}{\cosh(qA)} \tilde{\theta}_{gq}(0). \tag{4.9}$$

The solution for the perturbation in the vapour concentration is analogous,

$$\tilde{\zeta}_{vq}(\tilde{z}) = \frac{\cosh[q(\tilde{z} - A)]}{\cosh(qA)} \tilde{\zeta}_{vq}(0), \tag{4.10}$$

where $\tilde{\zeta}_{vq}(0)$ can be related to the perturbation in the interfacial temperature via the Clausius–Clapeyron relation (2.16)

$$\tilde{\zeta}_{vq}(0) = \tilde{\theta}_{gq}(0). \tag{4.11}$$

Fourier transforming (3.18) yields

$$\tilde{J}_q = -\frac{\Omega}{c_a^0} \tilde{\zeta}'_{vq}(0), \tag{4.12}$$

where \tilde{J}_q is the Fourier coefficient of $\tilde{J}(\tilde{x})$. Subtracting the base solutions from the heat balance (3.16), Fourier transforming the result, and using (4.12) gives the following relation

$$\tilde{\theta}'_{lq}(0) = \frac{k_g}{k_l} \tilde{\theta}'_{gq}(0) + \frac{\Omega}{c_a^0} \frac{V}{Ma} \tilde{\zeta}'_{vq}(0). \tag{4.13}$$

With the help of (4.9), (4.10) and (4.11) this can be rewritten in the form of Newton's cooling law

$$\tilde{\theta}'_{lq}(0) = -Bi_q \tilde{\theta}_{lq}(0), \tag{4.14}$$

where we introduced a wavenumber-dependent analogue of the Biot number

$$Bi_q = q \tanh(qA) \left[\frac{k_g}{k_l} + \frac{1 - c_a^0}{c_a^0} H \right], \tag{4.15}$$

which will be referred to as the Biot coefficient below to highlight the fact that it is a function of q and c_a^0 , not a constant. The prefactor $\tanh(qA)$ describes the effect of finite thickness of the gas layer. For $d_g \gg d_l$ ($A \gg 1$), it approaches unity and (4.15) reduces to the expression derived by Chauvet, Dehaeck & Colinet (2012) in the context of stability of a volatile liquid layer in the presence of a vertical temperature gradient. The first term describes the effect of thermal conduction through the gas layer, while the second term describes the effect of latent heat released/absorbed at the interface as a result of condensation/evaporation.

By linearizing the governing equations (3.10) around the base state (3.25)–(3.27), we obtain the evolution equations for the perturbations $\tilde{\psi}_{lq}$ and $\tilde{\theta}_{lq}$ in the liquid layer

$$\left. \begin{aligned} \tilde{\nabla}_q^2 \tilde{\nabla}_q^2 \tilde{\psi}_{lq} + iqC_1(\tilde{z}) Re \tilde{\psi}_{lq}'' - iqC_2(\tilde{z}) Re \tilde{\psi}_{lq} - iqGr \tilde{\theta}_{lq} &= \sigma_q \tilde{\nabla}_q^2 \tilde{\psi}_{lq}, \\ Pr^{-1} \tilde{\nabla}_q^2 \tilde{\theta}_{lq} + iqC_1(\tilde{z}) Re \tilde{\theta}_{lq} - iqC_3(\tilde{z}) Ma \tilde{\psi}_{lq} - \tilde{\psi}'_{lq} &= \sigma_q \tilde{\theta}_{lq}, \end{aligned} \right\} \tag{4.16}$$

where we defined $\tilde{\nabla}_q^2 = \partial_{\tilde{z}}^2 - q^2$ and

$$\left. \begin{aligned} C_1(\tilde{z}) &= \frac{(\tilde{z} + 1)(3\tilde{z} + 1)}{4} - Bo_D \frac{(\tilde{z} + 1)(8\tilde{z}^2 + \tilde{z} - 1)}{48}, \\ C_2(\tilde{z}) &= q^2 C_1(\tilde{z}) + \frac{3}{2} - Bo_D \frac{8\tilde{z} + 3}{8}, \\ C_3(\tilde{z}) &= \frac{\tilde{z}(\tilde{z} + 1)^2}{4} - Bo_D \frac{\tilde{z}(\tilde{z} + 1)^2(2\tilde{z} - 1)}{48}. \end{aligned} \right\} \tag{4.17}$$

This is a system of ODEs which is fourth order with respect to $\tilde{\psi}_{lq}$ and second order with respect to $\tilde{\theta}_{lq}$ and hence needs a total of six boundary conditions. These boundary conditions are:

$$\left. \begin{aligned} \tilde{\psi}_{lq}(-1) &= 0, \\ \tilde{\psi}'_{lq}(-1) &= 0, \\ \tilde{\theta}'_{lq}(-1) &= 0, \end{aligned} \right\} \tag{4.18}$$

at the bottom of the liquid layer and

$$\left. \begin{aligned} \tilde{\psi}_{lq}(0) &= 0, \\ \tilde{\psi}'_{lq}(0) &= -iqRe\tilde{\theta}_{lq}(0), \end{aligned} \right\} \tag{4.19}$$

and

$$\tilde{\theta}'_{lq}(0) = -Bi_q\tilde{\theta}_{lq}(0), \tag{4.20}$$

at the free surface. In the subsequent discussion we will refer to the system (4.16) with the boundary conditions (4.18)–(4.20) as the enhanced one-sided model, since it incorporates the effect of the gas phase entirely through boundary conditions at the interface.

4.2. Transient dynamics in the gas layer

A more accurate description of the instability, stationary or oscillatory, can be obtained by restoring the time dependence of the temperature and composition of the gas phase. This corresponds to replacing the Laplace equations (4.3) with

$$\left. \begin{aligned} \partial_t \tilde{T}_g &= K_\alpha \tilde{\nabla}^2 \tilde{T}_g, \\ \partial_t \tilde{c}_v &= K_D \tilde{\nabla}^2 \tilde{c}_v. \end{aligned} \right\} \tag{4.21}$$

The corresponding equations for the perturbations are

$$\left. \begin{aligned} \tilde{\psi}_{gq} &= 0, \\ \tilde{\theta}''_{gq} - q^2 \tilde{\theta}_{gq} &= \sigma_q K_\alpha^{-1} \tilde{\theta}_{gq}, \\ \tilde{\zeta}''_{vq} - q^2 \tilde{\zeta}_{vq} &= \sigma_q K_D^{-1} \tilde{\zeta}_{vq}. \end{aligned} \right\} \tag{4.22}$$

These equations should be solved subject to the boundary conditions (4.7), (4.8), (4.11), (4.18), (4.19) and

$$\tilde{\theta}'_{lq}(0) = -\frac{k_g}{k_l} \tilde{\theta}'_{gq}(0) - \frac{1 - c_a^0}{c_a^0} H \tilde{\zeta}'_{vq}(0), \tag{4.23}$$

which follows from the heat flux balance (3.16) and the mass flux balance (4.12) and replaces (4.14).

Since it involves an incomplete description of the gas layer (the effects of advection are not included), this model based on the governing equations (4.16) and (4.22) can be called ‘one-and-a-half-sided.’ Note that, since both K_α and K_D are typically large compared with unity, the terms on the right-hand side of (4.22) are small. Dropping them would lead to the enhanced one-sided model derived in §4.1.

4.3. The effect of advection in the gas layer

The effect of advection can also be incorporated for the range of c_a^0 where the base solution (3.35)–(3.38) is valid. By setting $\tilde{\psi}_{gq} \neq 0$ we ensure that all of the transport mechanisms in the gas phase are accounted for and both layers are treated using an

equally comprehensive model. The linearized evolution equations for the perturbations $\tilde{\psi}_{gq}$, $\tilde{\zeta}_{vq}$ and $\tilde{\theta}_{gq}$ in the gas phase are

$$\left. \begin{aligned} K_v \tilde{\nabla}_q^2 \tilde{\nabla}_q^2 \tilde{\psi}_{gq} + iq \tilde{C}_1(\tilde{z}) \mathcal{R} \tilde{\psi}_{gq}'' - iq \tilde{C}_2(\tilde{z}) \mathcal{R} \tilde{\psi}_{gq} - iq \Xi_T \tilde{\theta}_{gq} - iq \Xi_\zeta \tilde{\zeta}_{vq} &= \sigma_q \tilde{\nabla}_q^2 \tilde{\psi}_{gq}, \\ K_\alpha \tilde{\nabla}_q^2 \tilde{\theta}_{gq} + iq \tilde{C}_1(\tilde{z}) \mathcal{R} \tilde{\theta}_{gq} - iq \tilde{C}_3(\tilde{z}) \mathcal{R} K_\alpha^{-1} \tilde{\psi}_{gq} - \tilde{\psi}_{gq}' &= \sigma_q \tilde{\theta}_{gq}, \\ K_D \tilde{\nabla}_q^2 \tilde{\zeta}_{vq} + iq \tilde{C}_1(\tilde{z}) \mathcal{R} \tilde{\zeta}_{vq} - iq \tilde{C}_3(\tilde{z}) \mathcal{R} K_D^{-1} \tilde{\psi}_{gq} - \tilde{\psi}_{gq}' &= \sigma_q \tilde{\zeta}_{vq}, \end{aligned} \right\} \quad (4.24)$$

where

$$\left. \begin{aligned} \tilde{C}_1(\tilde{z}) &= \frac{(\tilde{z} - A)(3\tilde{z} - A)}{4A^2} + \mathcal{B} \frac{(\tilde{z} - A)(8\tilde{z}^2 - A\tilde{z} - A^2)}{48A^3}, \\ \tilde{C}_2(\tilde{z}) &= q^2 \tilde{C}_1(\tilde{z}) + \frac{3}{2A^2} + \mathcal{B} \frac{8\tilde{z} - 3A}{8A^3}, \\ \tilde{C}_3(\tilde{z}) &= \frac{\tilde{z}(\tilde{z} - A)^2}{4A^2} + \mathcal{B} \frac{\tilde{z}(\tilde{z} - A)^2(2\tilde{z} + A)}{48A^3}. \end{aligned} \right\} \quad (4.25)$$

The boundary conditions are given by (4.7), (4.8), (4.11), (4.18), (4.19) and (4.23). In addition, the boundary conditions for $\tilde{\psi}_{gq}(\tilde{z})$ follow from (3.21) and (3.22):

$$\left. \begin{aligned} \tilde{\psi}_{gq}(A) &= 0, \\ \tilde{\psi}_{gq}'(A) &= 0, \end{aligned} \right\} \quad (4.26)$$

at the top of the gas layer and

$$\left. \begin{aligned} \tilde{\psi}_{gq}(0) &= 0, \\ \tilde{\psi}_{gq}'(0) &= \tilde{\psi}_{lq}'(0), \end{aligned} \right\} \quad (4.27)$$

at the free surface. In the subsequent discussion we will refer to the system (4.16) and (4.24) with the appropriate boundary conditions as the two-sided model, since it treats both the liquid and the gas phase with the same level of detail.

4.4. Different modes of instability

The boundary value problem, whether it is described by the system (4.16) by itself or combined with (4.22) or (4.24), has a spectrum of eigenvalues σ_q^n and the corresponding eigenfunctions $\{\psi_{lq}^n, \theta_{lq}^n, \dots\}$, $n = 0, 1, \dots$, for a given complex wavenumber $q = k + is$ and Marangoni number Ma . The stability of the base flow is determined by the eigenvalue $\sigma_q^0 = \kappa_q + i\omega_q$ with the largest real part κ_q and the character of the instability (oscillatory or stationary) is determined by the imaginary part ω_q .

So far we have only focused on the boundary conditions in the vertical (confined) direction. In both experiment and simulations the fluid layers are also bounded in the horizontal (extended) directions $0 < x < L_x$ and $0 < y < L_y$. Comparison of various experimental results suggests that the spanwise aspect ratio $\Gamma_y = L_y/d_l$ is not particularly important: aside from the orientation of hydrothermal waves at low Bo_D , the pattern that emerges above the threshold of primary instability is basically the same for both $\Gamma_y = O(1)$ (Villers & Platten 1992; De Saeleer *et al.* 1996; Garcimartín *et al.* 1997; Li *et al.* 2014) and $\Gamma_y \gg 1$ (Riley & Neitzel 1998; Burguete *et al.* 2001). This is not very surprising since the boundaries in the spanwise direction play a passive role – they tend to suppress, rather than enhance convection.

The boundaries in the streamwise direction are less trivial and play a crucial role in selecting the convection pattern for any $\Gamma_x = L_x/d_l$. The corresponding boundary conditions are of the enhancing type (Cross & Greenside 2009): buoyancy, which plays a significant role for $Bo_D = O(1)$, drives an upward flow near the hot end wall, generating a single localized convection roll. Similarly, buoyancy drives a downward flow near the cold end wall, generating another, much weaker, convection roll. These rolls appear for Ma well below the critical value Ma_c at which convection pattern emerges away from the end walls. The rolls are steady over a wide range of Ma and have a horizontal extent of $O(d_l)$. For $\Gamma_x \gg 1$ and sufficiently low Ma , the flow in the core region between these two convection rolls, i.e. for $O(d_l) < x < L_x - O(d_l)$, is described well by the base flow solution (3.26) and (3.36), as mentioned previously (cf. figure 1). Riley & Neitzel (1998) refer to this state as a steady unicellular flow (SUF). Since the perturbation strength is always finite at the end walls, defining the threshold of the primary instability at finite Γ_x requires some care.

4.4.1. Convective instability

The dominant mode of primary instability in laterally unbounded systems (infinite Γ_x) tends to be convective. The threshold of convective instability corresponds to κ_q being negative over all q -real, except for $q = k_c$, where k_c is the (real) critical wavenumber which defines the wavelength $\lambda/d_l = 2\pi/k_c$ of the pattern that develops above threshold. Therefore, the critical wavenumber k_c and the critical Marangoni number Ma_c are given by the solution of the two equations

$$\left. \begin{aligned} \kappa_q|_{q_c} &= 0, \\ \frac{\partial \kappa_q}{\partial q}|_{q_c} &= 0, \end{aligned} \right\} \quad (4.28)$$

over q -real. Generally, the critical frequency $\omega_c = \omega_q|_{q_c} \neq 0$, so the resulting pattern will be oscillatory, with disturbances amplified in the frame of reference moving with the group velocity (Huerre 2000)

$$v_g = - \frac{\partial \omega_q}{\partial q} \Big|_{q_c}. \quad (4.29)$$

In laterally bounded systems, such as the fluid volumes with finite aspect ratios Γ_x discussed in this paper, convective instabilities should not be observed in the absence of a localized oscillatory source of the right temporal frequency ($\omega \approx \omega_c$). An example of such a source could be an oscillating convection roll near the left (right) end wall for $v_g > 0$ ($v_g < 0$) driven by a completely different mechanism (e.g. buoyancy due to cooling or heating at the end wall). While such oscillating convection rolls have indeed been observed in experiment (De Saedeleer *et al.* 1996; Garcimartín *et al.* 1997; Li *et al.* 2014) and simulations (Qin *et al.* 2014), they arise after convection pattern in the core region of the flow has already been established. Hence, this is a secondary, rather than a primary, instability. We should only expect to see a primary convective instability in systems with very large streamwise aspect ratio Γ_x where infinitesimal disturbances have sufficient time Γ_x/v_g to develop.

4.4.2. Absolute instability

Absolute instabilities arise when infinitesimal disturbances grow in the laboratory frame. Since they do not need a finite-amplitude source, they can arise both in laterally unbounded systems as well as in bounded systems with moderate Γ_x . Absolute instability requires that the group velocity $v_g = 0$ at onset, yielding a system of three real equations for three real unknown $k_c = \text{Re}(q_c)$, $s_c = \text{Im}(q_c)$, and Ma_c , which can be rewritten as a system of two equations (Huerre 2000)

$$\left. \begin{aligned} \kappa_q|_{q_c} &= 0, \\ \frac{\partial \sigma_q^0}{\partial q} \Big|_{q_c} &= 0, \end{aligned} \right\} \quad (4.30)$$

the second of which is complex, for q_c -complex and Ma_c .

The resulting pattern will generally be oscillatory, $\omega_c \neq 0$, just like in the case of convective instability. Although its group velocity vanishes, the phase velocity $v_p = -\omega_c/k_c$ of the pattern will be non-zero. A good example of such an absolute instability is hydrothermal waves (Smith & Davis 1983a,b) that are observed in the limit of low Bo_D (Daviaud & Vince 1993; Riley & Neitzel 1998; Burguete *et al.* 2001). In the following, where necessary to avoid confusion, we will use the superscript a to denote the critical values corresponding to absolute instability.

4.4.3. Stationary instability

The threshold of a stationary instability corresponds to both the real and imaginary part of σ_q^0 vanishing

$$\left. \begin{aligned} \kappa_q|_{q_c} &= 0, \\ \omega_q|_{q_c} &= 0. \end{aligned} \right\} \quad (4.31)$$

These two equations should be solved for the critical wavenumber k_c and the critical Marangoni number Ma_c , which both depend on the spatial attenuation rate s . In the following, where necessary to avoid confusion, we will use the superscript s to denote the critical values corresponding to stationary instability. In particular, we will write $Ma_c^s(s)$ to explicitly denote the dependence on s .

In laterally infinite systems the transition threshold is well defined and corresponds to a spatially uniform stationary pattern ($s = 0$). Such a pattern will be referred to as the steady multicellular (SMC) state below. For $Ma < Ma_c^s(0)$ the convection pattern arises due to forcing at one of the boundaries (convection rolls driven by buoyancy, cf. figure 1(c,d)), rather than spontaneously, and generally does not extend across the entire length of the system. In this case the absolute value of $s = \text{Im}(q_c)$ defines the spatial attenuation of the perturbation (or the number of convection rolls that can be detected in the liquid layer), while $k_c = \text{Re}(q_c)$ determines the wavelength λ of the pattern (or the distance between convection rolls). For $s \neq 0$ the pattern appears below $Ma_c^s(0)$ and is localized near the right (hot) end wall for $s < 0$ or near the left (cold) end wall for $s > 0$. As we will see below, $dMa_c^s/ds > 0$, which means that the pattern always appears near the hot end wall (cf. figure 1d) and we can only consider $s \leq 0$.

When $e^{-|s|L_x} \ll 1$, the pattern extends over a region of length $O(2d_l/|s|) < L_x$. We will refer to this as partial multicellular (PMC) state following Qin & Grigoriev (2015) and Li *et al.* (2014). In this analysis, we set $s_{PMC} = -1$ to define the transition from SUF to PMC at $Ma_c^s(-1) < Ma_c^s(0)$, which roughly corresponds to one extra roll nucleating near the (hot) end wall. As Ma is increased beyond this value,

the convection pattern extends further away from the end wall, until it eventually covers the entire fluid layer. In practice this roughly corresponds to $e^{-|s|\Gamma_x} \approx 0.1$ or $s_{SMC} = \pm 2/\Gamma_x$. This is the definition that has to be used for $Pr \lesssim 1$ (i.e. for gases or metallic liquids featuring sensitive dependence of Ma_c^s on s for small $|s|$, as shown below). For typical (non-metallic) liquids with $Pr = O(10)$, we can set $s_{SMC} = 0$, as in the case of laterally unbounded layers, as long as $\Gamma_x \gtrsim 20$. This is the case in both the experimental (Riley & Neitzel 1998; Li *et al.* 2014) and numerical studies (Qin *et al.* 2014; Qin & Grigoriev 2015) used for comparison below.

Note that, for $\sigma_q^0 = 0$, equations (4.22) reduce to (4.6) even if K_α and K_D are not large. Hence the two formulations always give identical predictions for the threshold of stationary instability (even though they predict different growth rates for modes with wavenumbers q different from the critical one). Therefore, in what follows we will only focus on the limits when either both Pe_m and Pe_t are vanishingly small and stability is described by (4.16) alone, or when they are both $O(1)$, so (4.16) and (4.24) have to be solved simultaneously.

5. Results

Previous theoretical studies of stability focused mainly on the dependence of the critical Marangoni number Ma on the dynamic Bond number Bo_D and Prandtl number Pr characterizing the liquid layer. We have also investigated how both the critical Ma and the critical wavelength λ depend on the equilibrium concentration c_a^0 of air in the gas layer. Where possible, the predictions of linear stability analysis have been compared with the available experimental and numerical data. The boundary value problems, which determine σ_q^0 as a function of the wavenumber q and various non-dimensional parameters, were solved using the function **bvp5c** in Matlab 2016a (cf. appendix A for details) and the equations (4.28), (4.30) and (4.31), defining the conditions for various types of instabilities where solved using the Newton method.

5.1. Convection at atmospheric conditions

The most comprehensive experimental study to date that investigated convection patterns in the problem considered here is due to Riley & Neitzel (1998), who determined the dependence of both the critical Ma and the critical wavelength λ corresponding to the onset of various instabilities on the dynamic Bond number Bo_D for the 1 cSt silicone oil with $Pr = 13.9$. Since the authors have not reported the values of all material parameters of the liquid, we took the missing ones from Kavehpour, Ovryn & McKinley (2002). No data has been found for the material properties of the vapour; these were assumed to be the same as those of the 0.65 cSt silicone oil (Yaws 2003, 2009). Any potential uncertainty in the values of these material parameters, however, will have a negligible effect on the results. The 1.0 cSt silicone oil is not particularly volatile (the saturation vapour pressure is $p_v = 0.5$ kPa at $T = 298$ K, which corresponds to $c_a^0 = 0.995$ at atmospheric conditions), therefore the properties of the gas phase are essentially those of air.

The predictions of the linear stability analysis for this particular fluid are shown in figures 3 and 4. The enhanced one-sided model and the two-sided model produce essentially identical results at atmospheric conditions; we only show the results of the latter. In particular, the thresholds of different types of instabilities for a laterally unbounded system ($\Gamma_x = \infty$) are shown as solid lines in figure 3(a). These are in decent agreement with the thresholds of convective, absolute, and stationary instabilities predicted by Priede & Gerbeth (1997) using an adiabatic one-sided model

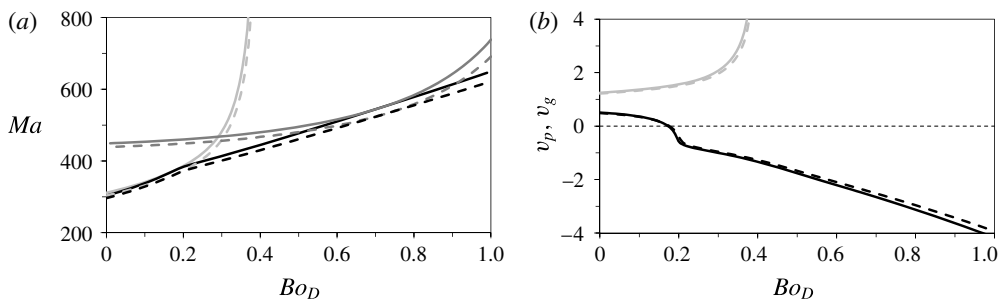


FIGURE 3. Different types of instability in a laterally infinite layer of 1.0 cSt silicone oil at atmospheric conditions ($c_a^0 = 0.995$) as a function of the dynamic Bond number. (a) Critical Ma for the absolute (light grey), stationary (dark grey), and convective (black) instability. (b) Group velocity v_g for convective instability (black) and phase velocity v_p for absolute instability (light grey). Analytical predictions of the two-sided model are shown as solid lines and the predictions of the one-sided model with $Bi_q = 0$ as dashed lines.

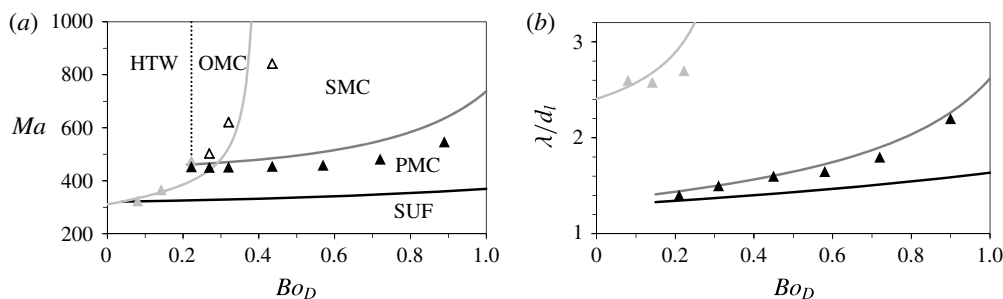


FIGURE 4. Dependence of the critical Marangoni number (a) and the critical wavelength (b) on the dynamic Bond number for the 1.0 cSt silicone oil at atmospheric conditions ($c_a^0 = 0.995$) in a layer with $L_x = 30$ mm. Experimental results obtained by Riley & Neitzel (1998) are shown as symbols (black filled for PMC/SMC, light grey filled for HTW, open for OMC). The boundary between HTW and OMC is shown as the dotted line. In both panels, analytical predictions of the two-sided model are shown as solid lines (light grey/dark grey/black for absolute instability/SMC/PMC threshold).

(which is equivalent to our enhanced one-sided model with $Bi_q = 0$). As expected, convective instability is predicted to occur at the lowest value of Ma regardless of Bo_D . Figure 3(b) shows the group velocity v_g associated with convective instability (along with the phase velocity v_p associated with absolute instability). In the absence of end walls, one should expect a pattern arising from convective instability to develop sooner on one side than the other, with the interface between patterned and unpatterned flow propagating in the direction controlled by the sign of v_g , i.e. in the direction of the thermal gradient for $Bo_D < 0.18$ and opposite the thermal gradient for $Bo_D > 0.18$.

In practice, the aspect ratio Γ_x is too low for convective instability to amplify tiny disturbances that are naturally present in the flow sufficiently so they could be observed before they collide with one of the walls and disappear. For instance, in the study of Riley & Neitzel (1998) $12 < \Gamma_x < 40$, while in most other experimental and numerical studies $\Gamma_x \leq 20$. As a result, convective instability would not be observed

(and will not be considered in detail here). Instead an absolute instability, a stationary instability, or a combination of both instabilities would occur, and the order in which these instabilities occur would determine the type of convection pattern. In particular, hydrothermal waves (HTW) are usually found for $Bo_D \rightarrow 0$ and a stationary pattern is found for $Bo_D = O(1)$. However, we are not aware of any studies that predict what the pattern might look like at the intermediate values of Bo_D . The analysis for large, but finite Γ_x (so there are end walls) is presented below.

Comparison of the theoretical predictions with the results of Riley & Neitzel (1998) is complicated by the fact that in the experimental study the transition threshold for SMC is identified as the instant when multiple convection rolls appear (near the hot end wall), but do not extend all the way to the cold end wall, which is not a very precise definition. However, the experimental data, which corresponds to an unknown value $-1 < s < 0$, should lie between the analytical prediction for the onset of PMC ($s = -1$) and SMC ($s = 0$). As shown in figure 4, both the critical Ma and the critical wavelength λ observed in the experiments are indeed bracketed by the theoretical values corresponding to the onset of PMC and SMC, and lie closer to the SMC boundary in the entire range of Bo_D investigated in the experiment, where stationary convective patterns are observed. Riley and Neitzel's supporting figures show the presence of numerous convection rolls at what they define to be the critical Ma , so their data points should indeed be closer to the SMC threshold than the PMC threshold.

For $Bo_D < 0.04$ the absolute instability boundary lies below that of PMC, $Ma_c^a < Ma_c^s(-1)$, so a pattern should appear at Ma_c^a over the entire extent of the fluid layer and feature travelling convection rolls, since $\omega_c \neq 0$. The predicted phase velocity is positive, which is consistent with hydrothermal waves that are known to propagate from the cold end wall to the hot end wall. All of this is in perfect agreement with the analysis of Smith & Davis (1983a) applicable in the limit $Bo_D \rightarrow 0$. Riley and Neitzel's experimental observations for $0.04 < Bo_D < 0.29$ deserve a separate discussion, since this is the range where the threshold of absolute instability lies between the PMC and SMC thresholds, $Ma_c^s(-1) > Ma_c^a > Ma_c^s(0)$. In this range the base flow can undergo an instability with respect to two different patterns in different regions. Consider the experimental protocol in which Ma is gradually increased at a fixed Bo_D . Our analysis predicts that a stationary pattern first develops near the hot end wall at the SMC threshold $Ma_c^s(-1)$. As Ma is increased beyond this value, the pattern spreads towards the cold end wall until Ma reaches the threshold Ma_c^a of absolute instability, which should cause hydrothermal waves to appear near the cold end wall. Hence the fraction of the fluid layer occupied by the two patterns should then depend on Bo_D and Γ_x , with HTW dominating for smaller Bo_D and PMC at higher Bo_D , which is qualitatively consistent with experimental observations. As figure 4(a) illustrates, our quantitative predictions for Ma_c and λ are also consistent with the experimental results in this range of Bo_D .

If Ma is increased further beyond $Ma_c^s(0)$, the SMC pattern itself eventually becomes unstable and is replaced by the oscillatory multicellular convection (OMC) state (Villers & Platten 1992; De Saedeleer *et al.* 1996; Garcimartín *et al.* 1997; Riley & Neitzel 1998; Qin *et al.* 2014). OMC features convection rolls travelling in the direction opposite to that of HTW, i.e. against thermal gradient, with the right-most convection roll acting as the oscillatory source of disturbance (Garcimartín *et al.* 1997; Qin *et al.* 2014; Li *et al.* 2014). While it may be tempting to associate the extension of the curve $Ma = Ma_c^a$ for $Bo_D > 0.29$ in figure 4(a) with the boundary between SMC and OMC, it is incorrect to do so, since the absolute instability

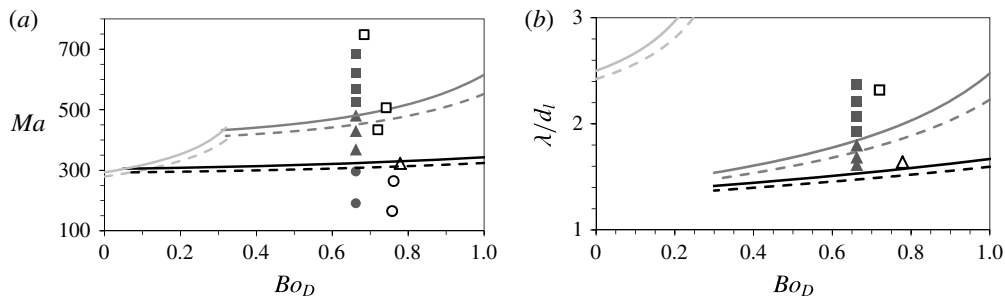


FIGURE 5. Dependence of the critical Marangoni number (a) and the critical wavelength (b) on the dynamic Bond number for the 0.65 cSt silicone oil at atmospheric conditions ($c_a^0 = 0.96$). Open symbols correspond to the experimental results of Li *et al.* (2014) and filled symbols correspond to the numerical results of Qin *et al.* (2014). The four distinct flow regimes are: SUF (\circ), PMC (\triangle), SMC (\square) and OMC (\diamond). In both panels, analytical predictions of the two-sided model are shown as solid lines (light grey/dark grey/black for absolute instability/SMC/PMC threshold). Predictions of the one-sided model with $Bi_q = 0$ are shown as dashed lines.

describes destabilization of the uniform base flow rather than the SMC pattern. On the other hand, the group velocity v_g associated with convective instability appears to predict the location of the boundary between HTW and OMC (the dashed line in figure 4a). As mentioned previously, $v_g > 0$ for $Bo_D < 0.18$, such that disturbances originating near the cold end wall should amplify as they propagate towards the hot end wall, while $v_g < 0$ for $Bo_D > 0.18$, so the opposite is true, which is consistent with the location of the wave sources for HTW and OMC. For comparison, in the experiment the boundary is at $Bo_D = 0.22$.

Next we compare the analytical predictions with the results of numerical and experimental studies (Li *et al.* 2014; Qin *et al.* 2014; Qin & Grigoriev 2015), which used a more volatile liquid (0.65 cSt silicone oil with $Pr = 9.2$) and characterized both the SMC \rightarrow PMC and the PMC \rightarrow SMC transition. The predicted dependence of the critical Marangoni number and wavelength on the dynamic Bond number at atmospheric conditions ($c_a^0 = 0.96$) is shown in figure 5. Again, the predictions of the enhanced one-sided and two-sided model are essentially indistinguishable and are in reasonable agreement with both experimental and numerical data. Just as in the case of 1 cSt silicone oil, the critical values of Ma and λ increase monotonically with Bo_D over the range where a stationary pattern is found ($Bo_D > 0.31$). This increase in Ma_c can be easily understood by noting that buoyancy has a stabilizing effect on the flow. The base flow solution (3.27) shows that the temperature increases, and hence the density of the liquid decreases, with height. An increase in Bo_D therefore corresponds to an increasingly strong effect of the stable density stratification.

At low Bo_D we again find that the absolute instability precedes the stationary instability, and we should expect to find HTW, at least near the cold end wall. According to figure 5(a), for $Bo_D < 0.05$, the threshold of absolute instability lies below the PMC threshold, $Ma_c^a < Ma_c^s(-1)$, so HTW should be observed over nearly the entire extent of the fluid layer. For $0.05 < Bo_D < 0.31$, the threshold of absolute instability lies between the PMC and SMC thresholds, $Ma_c^s(-1) < Ma_c^a < Ma_c^s(0)$. As we discussed previously, in this range we expect the two patterns to coexist for sufficiently large Γ_x , with the boundary between HTW and PMC at onset of the

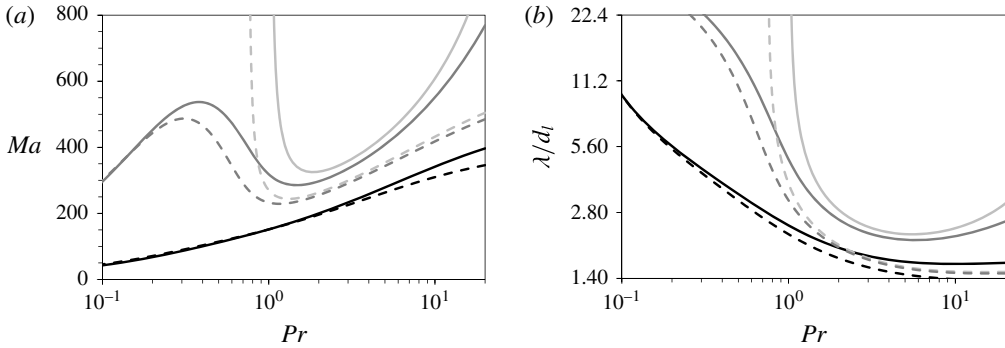


FIGURE 6. Stationary instability. Dependence of the critical Marangoni number (a) and the critical wavelength (b) on the Prandtl number of the liquid for $B_1 = 0.2$ and $c_a^0 \rightarrow 1$. The lines (solid for $Bo_D = 1$, dashed for $Bo_D = 0.3$) show the prediction of the enhanced one-sided model with $s = -1$ (black), $s = -0.1$ (dark grey) and $s = 0$ (light grey).

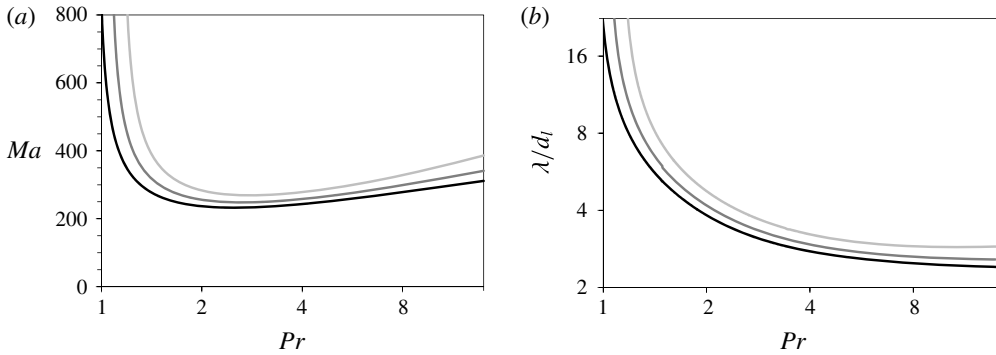


FIGURE 7. Absolute instability. Dependence of the critical Marangoni number (a) and wavelength (b) on the Prandtl number of the liquid for $B_1 = 0.2$ and $c_a^0 \rightarrow 1$. The lines show the prediction of the enhanced one-sided model for $Bo_D = 0$ (black), $Bo_D = 0.1$ (dark grey) and $Bo_D = 0.2$ (light grey).

absolute instability gradually shifting towards the cold end wall as Bo_D increases. The competition between these patterns above the threshold should be described by nonlinear theory and hence is not addressed here.

The dependence of the threshold values of Ma and λ on the Prandtl number of the liquid has previously been investigated only in the context of linear stability analysis. In particular, Priede & Gerbeth (1997), who only considered uniform disturbances ($s = 0$) and ignored heat and mass flux across the interface, found that the critical values of Ma for the stationary instability diverges at $Pr_0 = O(1)$ and reaches a minimum at Pr_1 just slightly higher than Pr_0 . (Oddly enough, they only show the data for $Bo_D = 0$, where HTW are expected instead of SMC.) Our enhanced one-sided model predicts that this result also holds for $Bo_D = O(1)$, once transport in the gas phase has been taken into account (cf. figure 6). The corresponding data for the absolute instability at lower Bo_D is shown in figure 7. Predictions of the two-sided model are not shown, since it involves too many parameters which will vary with Pr , as different Pr correspond to different liquids.

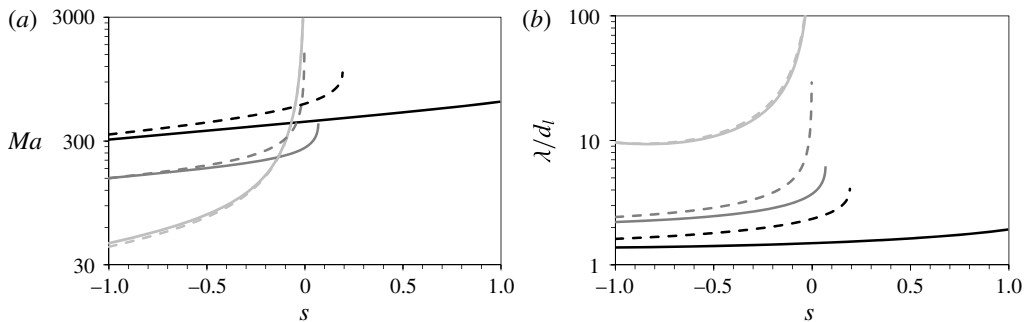


FIGURE 8. Stationary instability. Dependence of the critical Marangoni number (a) and wavelength (b) on the spatial attenuation rate for $c_a^0 \rightarrow 1$, $B_1 = 0.2$, and $Pr = 10$ (black), $Pr = 1$ (dark grey), or $Pr = 0.1$ (light grey). Solid lines correspond to the predictions of the enhanced one-sided model with $Bo_D = 0.3$ and dashed lines to $Bo_D = 1$.

Qualitatively similar trends are found for the threshold of SMC for all $Bo_D = O(1)$, with both Pr_0 and Pr_1 slowly increasing with Bo_D . Over the entire range of Pr corresponding to non-metallic liquids, Ma_c is a monotonically increasing function of Pr . The dependence of the critical wavelength on the Prandtl number is non-monotonic even for non-metallic liquids; λ has a minimum at $Pr_2 = O(10)$ and also diverges at Pr_0 . The divergence of the critical values of Ma and λ at Pr_0 , however, does not imply that no stationary pattern emerges at $Pr < Pr_0$. Indeed, the critical Ma for PMC ($s = -1$) decreases monotonically as Pr decreases, with $Ma_c \rightarrow 0$ as $Pr \rightarrow 0$. For instance, for a moderate value of $Ma \approx 600$, a stationary (spatially non-uniform) pattern is predicted to appear near the hot end wall for any $Pr < Pr_0$. As Ma increases, the spatial extent of the pattern should increase as well.

As noted in the introduction, the analysis of Mercier & Normand (2002) predicted that steady convection rolls should develop near the hot end for $Pr > 4$, near the cold end for $Pr < 0.01$, or at both end walls for $0.01 < Pr < 4$. Our results unequivocally contradict that prediction for $Bo_D = O(1)$. According to figure 6(b), for $Pr \lesssim 0.1$ the wavelength of the pattern exceeds typical values of Γ_x for any value of the spatial attenuation rate s , so it makes no sense to discuss spatial localization. (The dependence of the critical Ma and λ on s for the stationary instability at $Pr = 0.1$, 1 and 10 are shown in figure 8). We find that Ma_c^i is a monotonically increasing function of s , regardless of the values of Pr for $Bo_D = O(1)$, indicating that a stationary pattern always emerges first near the hot end wall.

The analysis of Mercier & Normand (2002) was performed mainly to understand the results of numerical simulations by Ban Hadid & Roux (1990) in the limit of low Pr which indicated the formation of a convective pattern near the cold end wall. Both of these studies made two contradicting assumptions: (i) that the dynamic Bond number $Bo_D \ll 1$ and (ii) that the liquid–gas interface is flat. As Smith & Davis (1983b) showed, in the limit $Bo_D \rightarrow 0$ the uniform base flow undergoes an instability towards surface waves for $Pr < 0.15$, violating the assumption of flat interface before a stationary instability can occur. Indeed, as figure 7(b) shows, even for finite Bo_D the critical wavelength associated with the absolute instability diverges as Pr approaches $Pr_0 = O(1)$ from above, indicating that for $Pr < Pr_0$ a long-wavelength instability will arise that necessarily causes substantial deformation of the interface. Even for $Pr > Pr_0$, no stationary pattern will appear near the cold end wall for small Bo_D , since the absolute instability precedes the stationary one, as figures 4 and 5 show.

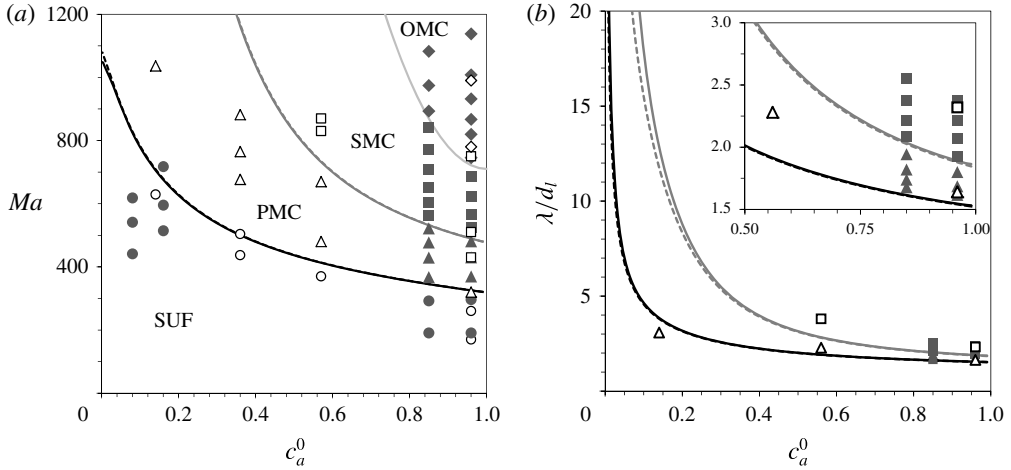


FIGURE 9. Dependence of the critical Marangoni number (a) and wavelength (b) on the average concentration of air for the 0.65 cSt silicone oil with $Bo_D = 0.7$. Solid (and dashed) lines are predictions of the two-sided (and enhanced one-sided) model for the thresholds of the PMC (black), SMC (dark grey) and OMC (light grey) patterns. The OMC threshold is a sketch based on numerical and experimental data. The meaning of the symbols is the same as that in figure 5. The inset in panel (b) shows the region of high c_a^0 and low λ .

In conclusion of this section, let us point out that even though phase change is greatly suppressed at atmospheric conditions, this does not mean that the effect of the gas phase is negligible. Figure 3 clearly shows the difference in the thresholds of all three instability types predicted by the adiabatic one-sided model (which completely ignores the effect of the gas layer) and the two-sided model (which accounts for heat, mass and momentum transport in the gas) for a fluid of relatively low volatility (1 cSt silicone oil). The difference is even more significant for the more volatile 0.65 cSt silicone oil, as figure 5 illustrates. We find that the one-sided model underestimates the critical values of both Ma and λ which correspond to the PMC/SMC boundary by between 4% at $Bo_D \approx 0.3$ and 11% at $Bo_D \approx 1$. The corresponding discrepancy for the absolute stability boundary ranges from 3% at $Bo_D = 0$ to 10% for $Bo_D \approx 0.3$. Not surprisingly, we find that transport of heat and mass through the gas phase delays all of the transitions. The effect of the gas phase increases rather dramatically, however, once the pressure is reduced below the atmospheric value, as we show below.

5.2. Convection at reduced pressures

In this section we will discuss the dependence of the critical Ma on the average concentration c_a^0 of air. We will focus exclusively on the 0.65 cSt silicone oil and $Bo_D = 0.7$, since relevant numerical and experimental data tend to cluster around that value. As we discussed previously, at this Bo_D the stationary instability dominates, so a time-independent pattern emerges. The one-sided model of Priede & Gerbeth (1997) does not account for phase change (recall that it corresponds to our enhanced one-sided model with $Bi_q = 0$), so its predictions are independent of c_a^0 . The predictions of the enhanced one-sided and the two-sided model are compared with available data in figure 9. The results of the two models are essentially identical, except for low

c_a^0 , where the validity of the assumptions underlying both models is questionable, as discussed below.

The predicted Ma_c increases rather significantly as c_a^0 is decreased from the atmospheric values down to the regime when the gas is dominated by the vapour, rather than air. The results of linear stability analysis are generally consistent with the experimental data, although at atmospheric conditions the predicted thresholds for the onset of PMC and SMC states are higher by about 20% compared with those found in experiment (cf. figure 9a). Numerical simulations have only been performed in the limits when either air or vapour dominate. When the gas phase is dominated by air ($c_a^0 \geq 0.85$), the predictions of linear stability analysis are consistent with the results of numerical simulations. When the vapour is dominant ($c_a^0 \leq 0.16$), the numerical simulations only find the SUF flow over the limited range of the imposed temperature gradients considered, so no prediction of Ma_c can be made. However, the corresponding lower bound supports the theoretical prediction that the threshold increases considerably.

The dependence of the critical wavelength on c_a^0 shows a trend similar to Ma_c : the predicted λ increases as c_a^0 decreases (cf. figure 9b). These predictions are in reasonable agreement with the available numerical and experimental results (Li *et al.* 2014; Qin & Grigoriev 2015). When the gas phase is dominated by air ($c_a^0 \geq 0.85$), the predicted critical wavelength for both the PMC and SMC state is in good agreement with the values found in the numerics and experiment. Only experimental data is available for lower c_a^0 , and again it is consistent with theoretical predictions for $c_a^0 > 0.3$: the wavelength of the pattern is found to lie between the PMC and SMC curves, as it should. For $c_a^0 < 0.16$ the critical wavelength becomes comparable to the length L of the cavity studied in Li *et al.* (2014), so some discrepancy between the theoretical predictions and the experimental results is expected.

In general, our linear stability analysis assumes a flat interface and will break down for $\lambda \gg d_l$ (i.e. at low c_a^0 and/or low Pr), when the thickness of the liquid layer is expected to vary noticeably. Furthermore, for sufficiently low c_a^0 and/or large Γ_x the interfacial temperature profile in the SUF state deviates significantly from linear, resulting in the breakdown of the analytical solution for the base flow (Qin & Grigoriev 2015). Therefore, the theoretical predictions in these limits are not expected to be particularly accurate.

6. Discussion

As our results illustrate, the predictions of the linear stability analysis based on the two-sided model are in general agreement with the reported numerical and experimental data. In particular, this analysis correctly predicts that the transitions between different flow regimes (SUF, PMC, SMC) are delayed (i.e. shifted towards higher Ma) when the concentration of air decreases, although quantitative agreement is not expected at low c_a^0 when the assumptions underlying our analysis become invalid. The general agreement found at higher c_a^0 confirms the validity of the assumptions made in the linear stability analysis, giving us confidence that it captures all the essential physical processes governing the flow stability for volatile liquids driven by a horizontal temperature gradient.

The predictions of linear stability analysis are consistent with the available numerical results. The discrepancy with the experiment can be due to a number of different reasons. One is the effect of transverse confinement: the liquid is wetting and rises at the sidewalls, increasing the thickness of the liquid layer there by up

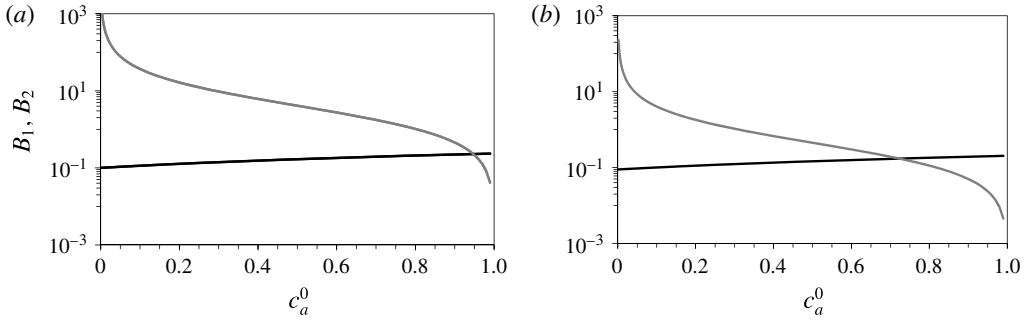


FIGURE 10. The role of heat and mass transport in the gas layer on flow stability for (a) the 0.65 cSt silicone oil and (b) the 1 cSt silicone oil. B_1 is shown as black and B_2 as grey line.

to 60%. The experimental study by Li *et al.* (2014) used the (smaller) thickness d_l of the liquid layer at the symmetry midplane $y = L_y/2$ of the cavity to compute Ma . Furthermore, the experimental study indirectly deduced the interfacial temperature gradient by comparing the experimental velocity profile with the analytical solution as in figure 2(a) rather than measure it directly, which introduces additional uncertainty into the reported values of Ma_c .

In this problem, buoyancy plays a stabilizing role, hence the instability leading to the formation of convection rolls is driven primarily by thermocapillary stresses, which depend on the interfacial temperature gradient. The fluctuations in the interfacial temperature are significantly affected by the heat and mass transport through the gas phase described – in the enhanced one-sided model – by the Biot coefficient Bi_q , which is a function of both the wavenumber q and the concentration of air c_a^0 . In particular, the first term in the square brackets in (4.15)

$$B_1 = \frac{k_g}{k_l} = \frac{c_a^0 k_a + (1 - c_a^0) k_v}{k_l} \tag{6.1}$$

describes the effect of conductive heat transport through the gas layer and reflects the dependence of thermal conductivity of the gas phase on its composition, while the second term

$$B_2 = \frac{1 - c_a^0}{c_a^0} H, \tag{6.2}$$

where H is the non-dimensional parameter defined by (3.31), describes the effect of the latent heat released or absorbed at the interface as a result of phase change and reflects the variation in the diffusive transport of vapour through the gas phase, which also depends on the gas composition. Both heat and mass transport through the gas phase suppress fluctuations in the interfacial temperature and hence play a stabilizing role.

To see the relative impact of the heat and mass transport on stability, it is instructive to compare the trends and characteristic magnitudes of the two terms. For the 0.65 cSt silicone oil, B_1 decreases slightly as c_a^0 decreases (thermal conductivity of the vapour is somewhat smaller than that of the air), but B_2 increases significantly, reflecting the enhancement of phase change (cf. figure 10). At atmospheric conditions, the heat flux in the gas phase has a slightly larger effect ($B_1 = 0.23$ versus $B_2 = 0.17$). The effect

of phase change becomes dominant for $c_a^0 < 0.95$ and increases as c_a^0 decreases. In fact, B_2 diverges as $c_a^0 \rightarrow 0$ which, according to (4.14), implies that the temperature fluctuations at the interface vanish and the critical Ma becomes infinite. The trends are similar for the less volatile 1 cSt silicone oil, although the effect of phase change is clearly weaker.

The increase in the critical Ma with decreasing c_a^0 is due primarily to the enhancement of phase change which increases the amount of latent heat released/absorbed by the warmer/cooler regions of the interface. Interestingly, the composition of the gas phase has a more significant effect on flow stability than the base flow itself. As discussed by Qin & Grigoriev (2015), the concentration of air has a relatively weak effect on the base flow, since the average interfacial temperature gradient, which determines the thermocapillary stresses, and hence the speed of the base flow, is insensitive to c_a^0 above 10% or so.

The one-sided model with the adiabatic boundary condition is ill-suited for describing the flow of volatile fluids. As discussed previously, even at atmospheric conditions, when phase change is strongly suppressed, it underestimates the critical Ma corresponding to all three instability types. At reduced pressures, phase change at the interface and heat and mass transport through the gas phase are all significantly enhanced, and predictions of the one-sided model become very inaccurate, since it completely fails to describe these effects. To illustrate the role of the gas phase, it is useful to focus on the dimensionless combinations that have been introduced over the years to describe the deviation from thermodynamic equilibrium, which gives rise to convection in the presence of evaporation. In particular, in their analysis of pure Marangoni (thermocapillary) instability in volatile fluids subjected to a vertical temperature gradient, Burelbach, Bankoff & Davis (1988) introduced two non-dimensional parameters: the evaporation number

$$E = \frac{k_l \Delta T}{\rho_l v_l \mathcal{L}}, \quad (6.3)$$

which defines the ratio of the evaporative time scale (how long it would take for a liquid layer to evaporate completely) to the viscous time scale, and the ‘non-equilibrium parameter’

$$K = \frac{2\chi}{2 - \chi} \sqrt{\frac{\bar{R}_v T_0 \rho_v \mathcal{L}^2 d_l}{2\pi k_l \bar{R}_v T_0^2}}, \quad (6.4)$$

which defines the ratio of the latent heat flux at the interface to the conductive heat flux in the liquid. The stability analysis of that problem was performed correctly only recently by Chauvet *et al.* (2012) who found that a version of the Biot coefficient (4.15) appears there as well. However, neither E nor K appears in the stability analysis, regardless of the direction of the temperature gradient, because both parameters fail to account for the transport (of either heat or mass) in the gas phase. Instead, the Biot coefficient involves a non-dimensional combination H which describes the effect of the latent heat associated with phase change and explicitly takes into account the mass transport in the gas phase.

The study by Normand, Pomeau & Velarde (1977) was probably the first to note that the Biot ‘number’ should depend on the wavenumber of the pattern for convective flows. In their analysis of buoyancy–thermocapillary convection driven by

a horizontal temperature gradient, Mercier & Normand (1996) repeated that statement, but proposed to use the definition

$$Bi = \frac{k_g d_l}{k_l d_g} \quad (6.5)$$

based on conduction in the two layers instead. Although wavenumber-independent, this definition is similar in form to the correct one in the combined limits of an infinitely thick gas layer and vanishing volatility. Indeed, if we ignore phase change, for $d_g \gg d_l$, the expression (4.15) would reduce to

$$Bi_q = q \frac{k_g}{k_l} = 2\pi \frac{k_g d_l}{k_l \lambda}. \quad (6.6)$$

Here the wavelength of the pattern effectively plays the role of the gas layer thickness, the result that follows immediately from the second equation in (4.3) which controls the heat transport in the gas phase.

The wavenumber dependence of the Biot coefficient (4.15) implies that, once transformed to the real space, Newton's cooling law

$$d_l \hat{\mathbf{n}} \cdot \nabla T_l = -Bi(T_i - T_0) \quad (6.7)$$

becomes invalid and has to be replaced by a spatially non-local relation between the interfacial temperature and the normal temperature gradient (or heat flux) in the liquid phase. Given that the Biot number (6.5) describes one-dimensional conduction, it is not surprising that (6.7) fails when spatial variation of the solution in the extended direction(s) is taken into account.

Finally, by comparing the results of linear stability analysis based on three models of the gas layer that incorporate varying levels of detail, we found that advection (of heat, mass, or momentum) plays a relatively minor role and can be ignored except for low c_a^0 (e.g. when vapour dominates in the gas phase). In this limit, the two-sided model, which accounts for advection in the gas layer, predicts a slightly higher critical Ma for the threshold of both PMC and SMC. The increased role of advection can be readily understood by considering the associated changes in the Péclet numbers (4.1) and (4.2). Both α_g and D are proportional to $p_g^{-1} \propto 1 - c_a^0$, so both Pe_m and Pe_t should increase with decreasing c_a^0 (even if we ignore the increase in the characteristic velocity of the gas associated with enhanced phase change). We should also expect advection to play a more important role for low Pr , since both Pe_m and Pe_t are proportional to $Re = Ma/Pr$. The enhanced advective transport in the gas phase at low c_a^0 or low Pr tends to suppress the variation in the temperature at the interface, the thermocapillary stresses, and hence the onset of convection.

7. Conclusions

As several recent experimental (Li *et al.* 2014) and numerical (Qin & Grigoriev 2015) studies have demonstrated, phase change has a rather dramatic effect on the stability of the flow in a layer of a volatile liquid (0.65 cSt silicone oil) driven by a horizontal temperature gradient. These studies showed that the onset of instability is delayed rather significantly when the phase change is enhanced by removing non-condensable gases, such as air, from the system. Linear stability analysis based on a model that takes heat and mass transport in the gas phase into account produces

results that are overall in good quantitative agreement with these studies. In particular, it confirms that the instability that is responsible for generating a pattern of convection rolls is caused by the thermocapillary stresses, while buoyancy in the liquid layer has a stabilizing effect.

The analysis also shows that phase change plays a very important role, with the magnitude of the effect described by the non-dimensional combination H defined by (3.31), the same combination that appears in the convection problem with a vertical, rather than horizontal, temperature gradient (Chauvet *et al.* 2012). The similarity of the two problems is not coincidental: due to the weakness of advective fluxes, the transport of heat and mass in the gas layer is primarily due to diffusion of the perturbations about the base state. This diffusive transport is independent of the direction of the thermal gradient, which mainly affects the base state.

Even when phase change is suppressed (e.g. at atmospheric conditions or for a fluid with relatively low volatility), we find that the gas phase can have a noticeable effect on the stability of the flow. Our analysis shows that the transport of heat in the gas layer can account for an increase of more than ten percent in the critical Marangoni number. The effect of heat transport through the gas layer has been traditionally described using the Newton cooling law, with the magnitude of the heat flux characterized by the Biot number. While this law may be a reasonable approximation for the base flow, it breaks down completely the moment convection rolls appear. In fact, heat transport in the gas phase has to be treated explicitly in order to obtain quantitatively accurate results in the entire range of parameters.

Acknowledgements

This work was supported in part by the National Science Foundation under grant no. CMMI-1511470.

Appendix A. Numerical solution of the boundary value problem

The boundary value solver **bvp5c** is designed to deal with systems of first-order ODEs, so the higher-order ODEs arising in the linear stability analysis were converted to this form.

A.1. Diffusion-dominated case

For the diffusion-dominated case, we converted the boundary value problem (4.16) to a system of six first-order ODEs

$$\left. \begin{aligned} y'_1 &= y_2, & y'_2 &= y_3, \\ y'_3 &= y_4, & y'_4 &= C_4(\tilde{z})y_1 + C_5(\tilde{z})y_3 + i Gr q y_5, \\ y'_5 &= y_6, & y'_6 &= C_6(\tilde{z})y_1 + P r y_2 + C_7(\tilde{z})y_5, \end{aligned} \right\} \tag{A 1}$$

where $y_1 = \tilde{\psi}_{lq}$, $y_5 = \tilde{\theta}_{lq}$, and

$$\begin{aligned} C_4(\tilde{z}) &= -i Gr \frac{q^3(\tilde{z} + 1)(8\tilde{z}^2 + \tilde{z} - 1)}{48} - i Gr q \frac{8\tilde{z} + 3}{8} \\ &+ i Re \frac{q^3(\tilde{z} + 1)(3\tilde{z} + 1) + 6q}{4} - q^2(q^2 + \sigma_q), \end{aligned} \tag{A 2}$$

$$\left. \begin{aligned} C_5(\tilde{z}) &= iGr \frac{q(\tilde{z} + 1)(8\tilde{z}^2 + \tilde{z} - 1)}{48} - iRe \frac{q(\tilde{z} + 1)(3\tilde{z} + 1)}{4} + 2q^2 + \sigma_q, \\ C_6(\tilde{z}) &= iMaPr qC_3(\tilde{z}), \\ C_7(\tilde{z}) &= -iMa qC_1(\tilde{z}) + \sigma_q Pr + q^2. \end{aligned} \right\} \quad (A 3)$$

Respectively, the boundary conditions become

$$\left. \begin{aligned} y_1(-1) &= 0, & y_1(0) &= 0, \\ y_2(-1) &= 0, & y_6(-1) &= 0, \\ y_3(0) + iqRe y_5(0) &= 0 \end{aligned} \right\} \quad (A 4)$$

and

$$y_6(0) + Bi_q y_5(0) = 0. \quad (A 5)$$

A.2. Transient dynamics in the gas layer

To avoid solving coupled boundary value problems (4.16) and (4.24) defined on adjacent domains, we remapped the domain of $\tilde{\theta}_{gq}$ and $\tilde{\zeta}_{vq}$ from $[0, A]$ to $[-1, 0]$ by defining $\bar{z} = -\tilde{z}/A$ and introducing two new functions $\bar{\theta}_{gq}(\bar{z}) = \tilde{\theta}_{gq}(-\tilde{z})$ and $\bar{\zeta}_{vq}(\bar{z}) = \tilde{\zeta}_{vq}(-\tilde{z})$. In terms of these new functions, the system (4.22) becomes

$$\left. \begin{aligned} A^{-2}\bar{\theta}_{gq}'' - q^2\bar{\theta}_{gq} &= \sigma_q K_\alpha^{-1}\bar{\theta}_{gq}, \\ A^{-2}\bar{\zeta}_{vq}'' - q^2\bar{\zeta}_{vq} &= \sigma_q K_D^{-1}\bar{\zeta}_{vq}, \end{aligned} \right\} \quad (A 6)$$

where the prime now denotes the derivative with respect to \bar{z} , and the boundary condition (4.23) is replaced with

$$A\tilde{\theta}'_{lq}(0) = -\frac{k_g}{k_l}\bar{\theta}'_{gq}(0) - \frac{1 - c_a^0}{c_a^0}H\bar{\zeta}'_{vq}(0). \quad (A 7)$$

Furthermore, the no-flux boundary conditions at the top of the gas layer become

$$\left. \begin{aligned} \bar{\theta}'_{gq}(-1) &= 0, \\ \bar{\zeta}'_{vq}(-1) &= 0. \end{aligned} \right\} \quad (A 8)$$

Temperature continuity and the local phase equilibrium (4.11) at the free surface yield

$$\left. \begin{aligned} \bar{\theta}_{gq}(0) &= \tilde{\theta}_{lq}(0), \\ \bar{\zeta}_{vq}(0) &= \tilde{\theta}_{gq}(0). \end{aligned} \right\} \quad (A 9)$$

Converting (A 6) into a system of first-order ODEs yields four additional equations

$$\left. \begin{aligned} y'_7 &= y_8, & y'_8 &= A^2(q^2 + K_\alpha^{-1}\sigma_q)y_7, \\ y'_9 &= y_{10}, & y'_{10} &= A^2(q^2 + K_D^{-1}\sigma_q)y_9, \end{aligned} \right\} \quad (A 10)$$

where $y_7 = \bar{\theta}_{gq}$ and $y_9 = \bar{\zeta}_{vq}$, which should be added to the system (A 1). The boundary conditions (A 4) remain and (A 5) is replaced with

$$\left. \begin{aligned} Ay_6(0) + \frac{k_g}{k_l}y_8(0) + \frac{1 - c_a^0}{c_a^0}Hy_{10}(0) &= 0, \\ y_7(0) &= y_5(0), & y_8(-1) &= 0, \\ y_9(0) &= y_5(0), & y_{10}(-1) &= 0. \end{aligned} \right\} \quad (A 11)$$

A.3. The effect of advection in the gas layer

Just like in the previous case, we introduce new functions $\bar{\theta}_{gq}(\bar{z}) = \tilde{\theta}_{gq}(-\bar{z})$, $\bar{\zeta}_{vq}(\bar{z}) = \tilde{\zeta}_{vq}(-\bar{z})$ and $\bar{\psi}_{gq}(\bar{z}) = \tilde{\psi}_{gq}(-\bar{z})$, so the system (4.24) becomes

$$\left. \begin{aligned} K_v \bar{\nabla}_q^2 \bar{\nabla}_q^2 \bar{\psi}_{gq} + iq \bar{C}_1(\bar{z}) \mathcal{R} A^{-2} \bar{\psi}_{gq}'' - iq \bar{C}_2(\bar{z}) \mathcal{R} \bar{\psi}_{gq} - iq \mathcal{E}_T \bar{\theta}_{gq} - iq \mathcal{E}_\zeta \bar{\zeta}_{vq} &= \sigma_q \bar{\nabla}_q^2 \bar{\psi}_{gq}, \\ K_\alpha \bar{\nabla}_q^2 \bar{\theta}_{gq} + iq \bar{C}_1(\bar{z}) \mathcal{R} \bar{\theta}_{gq} - iq \bar{C}_3(\bar{z}) \mathcal{R} K_\alpha^{-1} \bar{\psi}_{gq} + A^{-1} \bar{\psi}_{gq}' &= \sigma_q \bar{\theta}_{gq}, \\ K_D \bar{\nabla}_q^2 \bar{\zeta}_{vq} + iq \bar{C}_1(\bar{z}) \mathcal{R} \bar{\zeta}_{vq} - iq \bar{C}_3(\bar{z}) \mathcal{R} K_D^{-1} \bar{\psi}_{gq} + A^{-1} \bar{\psi}_{gq}' &= \sigma_q \bar{\zeta}_{vq}, \end{aligned} \right\} \tag{A 12}$$

where we have defined $\bar{\nabla}_q^2 = A^{-2} \partial_{\bar{z}}^2 - q^2$ and

$$\left. \begin{aligned} \bar{C}_1(\bar{z}) &= \frac{(\bar{z} + 1)(3\bar{z} + 1)}{4} - \mathcal{B} \frac{(\bar{z} + 1)(8\bar{z}^2 + \bar{z} - 1)}{48}, \\ \bar{C}_2(\bar{z}) &= q^2 \bar{C}_1(\bar{z}) + \frac{3}{2A^2} - \mathcal{B} \frac{8\bar{z} + 3}{8A^2}, \\ \bar{C}_3(\bar{z}) &= -\frac{A\bar{z}(\bar{z} + 1)^2}{4} + \mathcal{B} \frac{A\bar{z}(\bar{z} + 1)^2(2\bar{z} - 1)}{48}. \end{aligned} \right\} \tag{A 13}$$

The functions $\bar{\zeta}_{vq}(\bar{z})$ and $\bar{\theta}_{gq}(\bar{z})$ again satisfy the boundary conditions (A 8) and (A 9). The boundary conditions for the function $\bar{\psi}_{gq}(\bar{z})$ follow from (3.21) and (3.22):

$$\left. \begin{aligned} \bar{\psi}_{gq}(-1) &= 0, \quad \bar{\psi}'_{gq}(-1) = 0, \\ \bar{\psi}_{gq}(0) &= 0, \quad \bar{\psi}'_{gq}(0) = -A \bar{\psi}'_{lq}(0). \end{aligned} \right\} \tag{A 14}$$

Converting (A 12) into a system of first-order ODEs yields eight additional equations

$$\left. \begin{aligned} y_7' &= y_8, \quad y_8' = \bar{C}_4(\bar{z})y_7 + iqA^2 \mathcal{R} K_\alpha^{-2} \bar{C}_3(\bar{z})y_{11} - AK_\alpha^{-1}y_{12}, \\ y_9' &= y_{10}, \quad y_{10}' = \bar{C}_5(\bar{z})y_9 + iqA^2 \mathcal{R} K_D^{-2} \bar{C}_3(\bar{z})y_{11} - AK_D^{-1}y_{12}, \\ y_{11}' &= y_{12}, \quad y_{12}' = y_{13}, \\ y_{13}' &= y_{14}, \quad y_{14}' = iqA^4 K_v^{-1}(\mathcal{E}_T y_7 + \mathcal{E}_\zeta y_9) + \bar{C}_6 y_{11} + \bar{C}_7 y_{13}, \end{aligned} \right\} \tag{A 15}$$

which augment the system (A 1) describing the liquid layer. Here $y_7 = \bar{\theta}_{gq}$, $y_9 = \bar{\zeta}_{vq}$, $y_{11} = \bar{\psi}_{gq}$, and

$$\left. \begin{aligned} \bar{C}_4(\bar{z}) &= -iqA^2 \mathcal{R} K_\alpha^{-1} \bar{C}_1(\bar{z}) + A^2(q^2 + K_\alpha^{-1} \sigma_q), \\ \bar{C}_5(\bar{z}) &= -iqA^2 \mathcal{R} K_D^{-1} \bar{C}_1(\bar{z}) + A^2(q^2 + K_D^{-1} \sigma_q), \\ \bar{C}_6(\bar{z}) &= iqA^4 \mathcal{R} K_v^{-1} \bar{C}_2(\bar{z}) - A^4 q^2(q^2 + K_v^{-1} \sigma_q), \\ \bar{C}_7(\bar{z}) &= -iqA^2 \mathcal{R} K_v^{-1} \bar{C}_1(\bar{z}) + A^2(2q^2 + K_v^{-1} \sigma_q). \end{aligned} \right\} \tag{A 16}$$

The boundary conditions are given by (A 4), (A 11), and

$$\left. \begin{aligned} y_{11}(0) &= 0, \quad y_{11}(-1) = 0, \\ y_{12}(0) &= -Ay_2(0), \quad y_{12}(-1) = 0. \end{aligned} \right\} \tag{A 17}$$

In all of the expressions given in the appendix, the non-dimensional parameters Re , Gr , \mathcal{R} , \mathcal{B} , \mathcal{E}_T and \mathcal{E}_ζ were expressed in terms of Ma , Pr , Bo_D and c_a^0 using the

definitions (3.3), (3.5), (3.7), (3.15), (3.30), (3.39) and (3.40). Similarly, parameters K_D , K_α and K_ν were evaluated as functions of c_a^0 .

REFERENCES

- BAN HADID, H. & ROUX, B. 1990 Thermocapillary convection in long horizontal layers of low-Prandtl-number melts subject to a horizontal temperature gradient. *J. Fluid Mech.* **221**, 77–103.
- BEN HADID, H. & ROUX, B. 1992 Buoyancy- and thermocapillary-driven flows in differentially heated cavities for low-Prandtl-number fluids. *J. Fluid Mech.* **235**, 1–36.
- BIRIKH, R. V. 1966 Thermocapillary convection in a horizontal layer of liquid. *Trans. ASME J. Appl. Mech. Tech. Phys.* **7**, 43–44.
- BURELBACH, J. P., BANKOFF, S. G. & DAVIS, S. H. 1988 Nonlinear stability of evaporating/condensing liquid films. *J. Fluid Mech.* **195**, 463–494.
- BURGUETE, J., MUKOLOBWIEZ, N., DAVIAUD, F., GARNIER, N. & CHIFFAUDEL, A. 2001 Buoyant-thermocapillary instabilities in extended liquid layers subjected to a horizontal temperature gradient. *Phys. Fluids* **13**, 2773–2787.
- CHAN, C. L. & CHEN, C. F. 2010 Effect of gravity on the stability of thermocapillary convection in a horizontal fluid layer. *J. Fluid Mech.* **647**, 91–103.
- CHAUVET, F., DEHAECK, S. & COLINET, P. 2012 Threshold of Benard–Marangoni instability in drying liquid films. *Europhys. Lett.* **99**, 34001.
- CROSS, M. C. & GREENSIDE, H. 2009 *Pattern Formation and Dynamics in Nonequilibrium Systems*. Cambridge University Press.
- DAVIAUD, F. & VINCE, J. M. 1993 Traveling waves in a fluid layer subjected to a horizontal temperature gradient. *Phys. Rev. E* **48**, 4432–4436.
- DE SAEDELEER, C., GARCIMARTÍN, A., CHAVEPEYER, G., PLATTEN, J. K. & LEBON, G. 1996 The instability of a liquid layer heated from the side when the upper surface is open to air. *Phys. Fluids* **8**, 670–676.
- GARCIMARTÍN, A., MUKOLOBWIEZ, N. & DAVIAUD, F. 1997 Origin of waves in surface-tension-driven convection. *Phys. Rev. E* **56**, 1699–1705.
- HA, J. M. & PETERSON, G. P. 1994 Analytical prediction of the axial dryout point for evaporating liquids in triangular microgrooves. *ASME J. Heat Transfer* **116**, 498–503.
- HUERRE, P. 2000 Open shear flow instabilities. In *Perspectives in Fluid Dynamics: A Collective Introduction to Current Research* (ed. G. K. Batchelor, H. K. Moffatt & M. G. Worster), pp. 159–229. Cambridge University Press.
- JI, Y., LIU, Q.-S. & LIU, R. 2008 Coupling of evaporation and thermocapillary convection in a liquid layer with mass and heat exchanging interface. *Chin. Phys. Lett.* **25**, 608–611.
- KAVEHPUR, P., OVRYN, B. & MCKINLEY, G. H. 2002 Evaporatively-driven Marangoni instabilities of volatile liquid films spreading on thermally conductive substrates. *Colloids Surf. A* **206**, 409–423.
- KIRDYASHKIN, A. G. 1984 Thermogravitational and thermocapillary flows in a horizontal liquid layer under the conditions of a horizontal temperature gradient. *Intl J. Heat Mass Transfer* **27**, 1205–1218.
- KLENTZMAN, J. & AJAEV, V. S. 2009 The effect of evaporation on fingering instabilities. *Phys. Fluids* **21**, 122101.
- LI, Y., GRIGORIEV, R. O. & YODA, M. 2014 Experimental study of the effect of noncondensables on buoyancy-thermocapillary convection in a volatile low-viscosity silicone oil. *Phys. Fluids* **26**, 122112.
- LI, Y.-R., ZHANG, H.-R., WU, C.-M. & XU, J.-L. 2012 Effect of vertical heat transfer on thermocapillary convection in an open shallow rectangular cavity. *Heat Mass Transfer* **48**, 241–251.
- LU, X. & ZHUANG, L. 1998 Numerical study of buoyancy- and thermocapillary-driven flows in a cavity. *Acta Mechanica Sin.* **14**, 130–138.

- MARKOS, M., AJAEV, V. S. & HOMSY, G. M. 2006 Steady flow and evaporation of a volatile liquid in a wedge. *Phys. Fluids* **18**, 092102.
- MERCIER, J. & NORMAND, C. 2002 Influence of the Prandtl number on the location of recirculation eddies in thermocapillary flows. *Intl J. Heat Mass Transfer* **45**, 793–801.
- MERCIER, J. F. & NORMAND, C. 1996 Buoyant-thermocapillary instabilities of differentially heated liquid layers. *Phys. Fluids* **8**, 1433–1445.
- MUNDRANE, M. & ZEBIB, A. 1994 Oscillatory buoyant thermocapillary flow. *Phys. Fluids* **6**, 3294–3306.
- NORMAND, C., POMEAU, Y. & VELARDE, M. 1977 Convective instability: a physicist's approach. *Rev. Mod. Phys.* **49**, 581–624.
- PARMENTIER, P. M., REGNIER, V. C. & LEBON, G. 1993 Buoyant-thermocapillary instabilities in medium-Prandtl-number fluid layers subject to a horizontal gradient. *Intl J. Heat Mass Transfer* **36**, 2417–2427.
- PRIEDE, J. & GERBETH, G. 1997 Convective, absolute, and global instabilities of thermocapillary-buoyancy convection in extended layers. *Phys. Rev. E* **56**, 4187–4199.
- QIN, T. & GRIGORIEV, R. O. 2015 The effect of noncondensables on buoyancy-thermocapillary convection of volatile fluids in confined geometries. *Intl J. Heat Mass Transfer* **90**, 678–688.
- QIN, T., TUKOVIĆ, Ž. & GRIGORIEV, R. O. 2014 Buoyancy-thermocapillary convection of volatile fluids under atmospheric conditions. *Intl J. Heat Mass Transfer* **75**, 284–301.
- QIN, T., TUKOVIĆ, Ž. & GRIGORIEV, R. O. 2015 Buoyancy-thermocapillary convection of volatile fluids under their vapors. *Intl J. Heat Mass Transfer* **80**, 38–49.
- RILEY, R. J. & NEITZEL, G. P. 1998 Instability of thermocapillary buoyancy convection in shallow layers. Part 1. Characterization of steady and oscillatory instabilities. *J. Fluid Mech.* **359**, 143–164.
- SCHATZ, M. F. & NEITZEL, G. P. 2001 Experiments on thermocapillary instabilities. *Annu. Rev. Fluid Mech.* **33**, 93–127.
- SCHRAGE, R. W. 1953 *A Theoretical Study of Interface Mass Transfer*. Columbia University Press.
- SHEVTSOVA, V. M. & LEGROS, J. C. 2003 Instability in thin layer of liquid confined between rigid walls at different temperatures. *Acta Astron.* **52**, 541–549.
- SHEVTSOVA, V. M., NEPOMNYASHCHY, A. A. & LEGROS, J. C. 2003 Thermocapillary-buoyancy convection in a shallow cavity heated from the side. *Phys. Rev. E* **67**, 066308.
- SMITH, M. K. & DAVIS, S. H. 1983a Instabilities of dynamic thermocapillary liquid layers. Part 1. Convective instabilities. *J. Fluid Mech.* **132**, 119–144.
- SMITH, M. K. & DAVIS, S. H. 1983b Instabilities of dynamic thermocapillary liquid layers. Part 2. Surface-wave instabilities. *J. Fluid Mech.* **132**, 145–162.
- SUMAN, B. & KUMAR, P. 2005 An analytical model for fluid flow and heat transfer in a micro-heat pipe of polygonal shape. *Intl J. Heat Mass Transfer* **48**, 4498–4509.
- VILLERS, D. & PLATTEN, J. K. 1987 Separation of marangoni convection from gravitational convection in earth experiments. *Phys. Chem. Hydrodyn.* **8**, 173–183.
- VILLERS, D. & PLATTEN, J. K. 1992 Coupled buoyancy and marangoni convection in acetone: experiments and comparison with numerical simulations. *J. Fluid Mech.* **234**, 487–510.
- YAWS, C. L. 2003 *Yaws' Handbook of Thermodynamic and Physical Properties of Chemical Compounds (Electronic Edition): Physical, Thermodynamic and Transport Properties for 5,000 Organic Chemical Compounds*. Knovel.
- YAWS, C. L. 2009 *Yaws' Thermophysical Properties of Chemicals and Hydrocarbons (Electronic Edition)*. Knovel.